THE JOURNAL OF PHYSICAL CHEMISTRY B
A JOURNAL OF THE AMERICAN CHEMICAL SOCIETY

pubs.acs.org/JPCB

Article

From Protein Design to the Energy Landscape of a Cold Unfolding Protein

Surya V. S. R. K. Pulavarti, Jack B. Maguire, Shirley Yuen, Joseph S. Harrison, Jermel Griffin, Lakshmanane Premkumar, Edward A. Esposito, George I. Makhatadze, Angel E. Garcia, Thomas M. Weiss, Edward H. Snell, Brian Kuhlman, and Thomas Szyperski*

Cite This: *J. Phys. Chem. B* 2022, 126, 1212–1231

Read Online

ACCESS | Metrics & More | Article Recommendations | Supporting Information

ABSTRACT: Understanding protein folding is crucial for protein sciences. The conformational spaces and energy landscapes of cold (unfolded) protein states, as well as the associated transitions, are hardly explored. Furthermore, it is not known how structure relates to the cooperativity of cold transitions, if cold and heat unfolded states are thermodynamically similar, and if cold states play important roles for protein function. We created the cold unfolding 4-helix bundle DCUB1 with a de novo designed bipartite hydrophilic/hydrophobic core featuring a hydrogen bond network which extends across the bundle in order to study the relative importance of hydrophobic versus hydrophilic protein−water interactions for cold unfolding. Structural and thermodynamic characterization resulted in the discovery of a complex energy landscape for cold transitions, while the heat unfolded state is a random coil. Below ∼0 °C, the core of DCUB1 disintegrates in a largely cooperative manner, while a near-native helical content is retained. The resulting cold core-unfolded state is compact and features extensive internal dynamics. Below −5 °C, two additional cold transitions are seen, that is, (i) the formation of a water-mediated, compact, and highly dynamic dimer, and (ii) the onset of cold helix unfolding decoupled from cold core unfolding. Our results suggest that cold unfolding is initiated by the intrusion of water into the hydrophilic core network and that cooperativity can be tuned by varying the number of core hydrogen bond networks. Protein design has proven to be invaluable to explore the energy landscapes of cold states and to robustly test related theories.

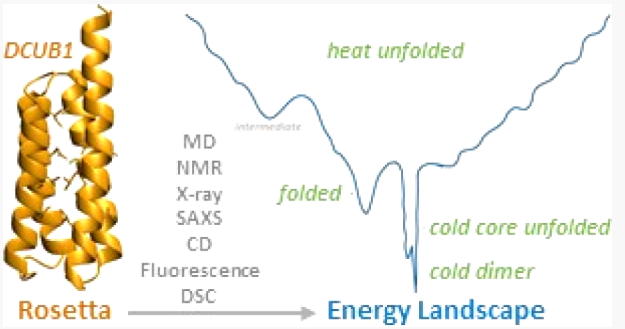

INTRODUCTION

Our understanding of the driving forces of protein folding[1] is crucial for protein science, structural biology, and biomedical research. Tremendous progress has been made to compute atomic resolution structures of folded proteins from the sequence.[2,3] In contrast, no theory exists to predict structural features of partially unfolded states or folding intermediates, or folding kinetics and thermodynamics.[4] The same holds for conformational states which are lowly populated under conditions when a protein is folded. Those can be of functional importance.[5−7] Although the phenomenon of protein cold unfolding has been known since the beginning of protein sciences,[8] cold transitions and cold (unfolded) states are significantly less well understood than their heat congeners. Here, we study distinct macrostates associated with the energy landscape[9,10] of a cold unfolding protein.

When compared to the folded macrostate,[7] protein heat unfolding leads to the formation of a macrostate associated with a microcanonical ensemble of higher energy E and higher entropy S ("HEHS state"). In contrast, cold unfolding[8,11,12] results in a macrostate associated with a microcanonical ensemble of lower E and lower S ("LELS state"). Protein and water molecules form a strongly coupled system,[13,14] and the crucial role of water for the formation of both heat and cold unfolded states is widely recognized.[15] There are two distinct types of ordered water molecules in the presence of proteins. In the case of cold unfolding, solvent exposure of hydrophobic surfaces leads to the formation of ordered, strongly hydrogen bonded and thus energetically favorable networks of water molecules[16−18] which feature a hallmark of the LELS cold unfolded state of proteins with a predominantly hydrophobic core. Hydrophilic protein−water interactions may likewise result in ordered, strongly hydrogen bonded water molecules at low temperatures. In general, however, the relative importance of these two types of ordered water molecules (i.e., networks of surface water molecules on hydrophobic surfaces vs water

Received: December 22, 2021
Revised: January 16, 2022
Published: February 7, 2022

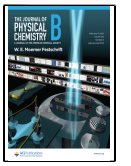

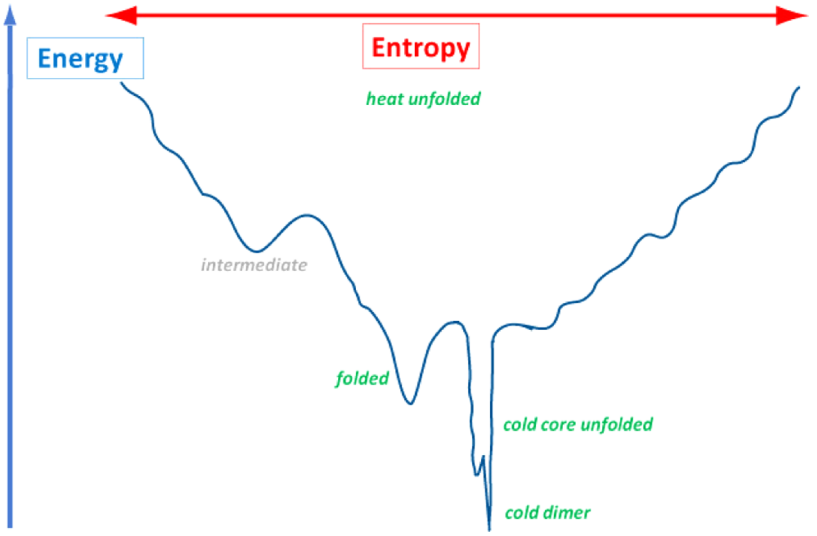

Figure 1. Schematic representation of the energy landscape[10] of DCUB1 inferred from experimental data. The HEHS heat unfolded state, the HEHS heat unfolding intermediate, the folded state, the LELS cold core-unfolded state, and the LELS cold dimer are indicated. Note that the dimer formation involves intermolecular contacts. For simplicity, the landscape was not expanded accordingly.[30]

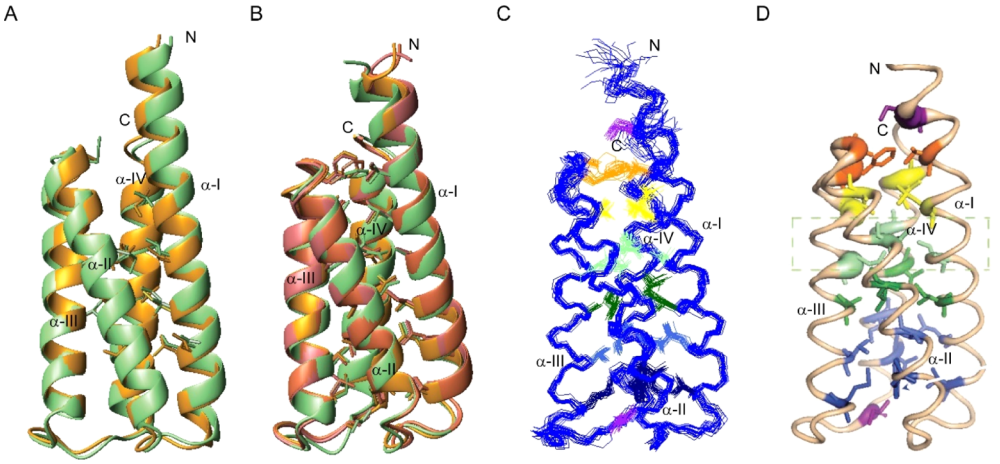

Figure 2. (A) Ribbon representation of the superposition of the DRNN X-ray structure chain-A (PDB ID 3U3B, in green) and DCUB1 Rosetta design model (in orange). The sidechains of the 16 residues that were replaced in DRNN to design DCUB1 (Figure S1.1) are depicted in neon. (B) Ribbon representation of the superposition of the DCUB1 X-ray structure (PDB ID 7T2Y, chain-A and chain-B in brown and orange) and lowest energy NMR conformer (PDB ID 7T03, in green). Core residues are depicted in neon. (C) Line representation of the backbone and core sidechains of 20 conformers representing the DCUB1 solution NMR structure. The hydrogen bond network in layer 3 is colored in green and highlighted with a dashed green box. All other core residues are hydrophobic. The color coding of the six layers in the core of DCUB1 is layer 1 (top; orange): residues 11, 57, and 58; layer 2: residues 15, 53, 61, and 101; layer 3 (green; H-bond network): 19, 49, 65, and 97; layer 4: 22, 46, 68, and 94; layer 5: 26, 42, 72, and 90; and layer 6: 29, 39, 75, and 87. (D) Gradient of the internal core mobility inferred from core sidechain root mean square fluctuation (RMSF) values (Table S2.4) obtained from DCUB1 MD simulations (Table S2.1), with a "sausage representation" for the backbone C^{α} atoms and the core sidechain heavy atoms displayed in a stick representation. The thickness of the spline curve of the backbone is proportional to the RMSF of core sidechain heavy atoms. As indicated by the green cone, core residues display smoothly decreasing RMSF values from the top to the bottom of the bundle. The hydrogen bond network in layer 3 is highlighted with a dashed green box.

molecules exhibiting hydrophilic interactions with the protein) has long been a matter of debate.[17,19,20]

Structural features determining the degree of cooperativity[21−23] of cold unfolding transitions are largely unknown. We suggest that the relative importance of the two types of ordered water molecules play a key role in determining the cooperativity of cold unfolding: the formation of energetically favorable networks of water molecules on hydrophobic surfaces is inherently a cooperative process, while even a single water molecule can be ordered through multiple hydrophilic interactions within the protein core. Hence, the formation of surface networks is likely to result in pronounced cooperativity, while the hydrophilic ordering of water molecules may proceed either in a cooperative or a non-cooperative manner by successive ordering of individual water molecules in the core.

Insights into protein cold unfolding studies are highly complementary to studies relying on the perturbation of other variables of state: for the characterization of a protein's energy landscape[9,10] (Figure 1) and cold LELS states are potentially as important as heat HEHS states. In general, states which are lowly populated (i.e., exhibit increased free energy) under conditions when a protein is folded may be either LELS or HEHS states, and they may both represent folding

https://doi.org/10.1021/acs.jpcb.1c10750
J. Phys. Chem. B 2022, 126, 1212−1231

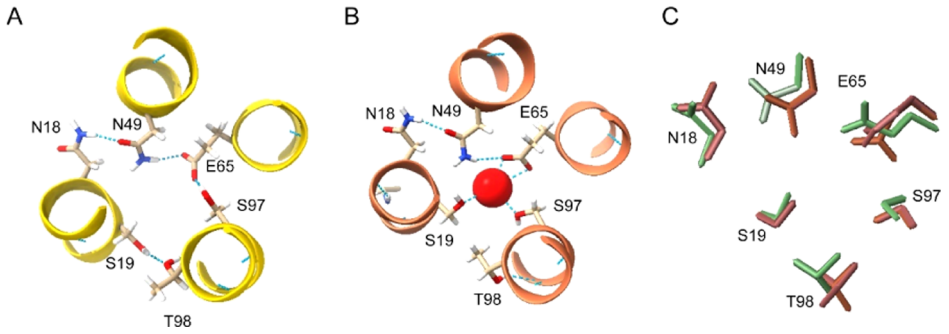

Figure 3. View from the top of the bundle (Figure 2) on the internal H-bond network of DCUB1. Helical segments are represented as ribbons and H-bonds are depicted as dotted lines. (A) Rosetta design model. (B) X-ray with the internal water (red sphere; Figure S4.2). (C) Superposition of X-ray structure (brown) and lowest energy NMR conformer (green).

intermediates or alternate conformations of the folded state which may be of functional importance. To distinguish between them, the *T*-dependence of populations needs to be measured.[24] In selected cases, such measurements were performed and it has been shown that ambient *T* lowly populated states are (partially) heat unfolded HEHS states.[25−28] However, in many cases, it is not evident if the experimental characterization of lowly populated states [primarily by nuclear magnetic resonance (NMR)[29]] captures cold LELS or heat HEHS states.

The experimental characterization of protein cold unfolding using high-resolution techniques is greatly impeded by the fact that most naturally occurring proteins are predicted to cold unfold far below the freezing point of water. While the use of capillaries allows the extension of the experimental *T*-range down to about −15 °C,[24,31−36] this is not sufficient for most naturally occurring proteins. Furthermore, it is imperative that chemical denaturants, which denature the genuine cold unfolded states, and/or extreme pH values are avoided.[37−39] As a result, the cold unfolded states of only five "model proteins" [91-residue CTL9(L98A),[37,40−43] 111-residue yeast frataxin yfh1,[18,38,44−46] dimeric 66-residue CylR2,[36] 126-residue apo-IscU(D39A),[39] and 91-residue HIV1 protease monomer[47]] have been characterized at a higher resolution under near physiological conditions. Of these, only dimeric CylR2 was studied in a supercooled water well below 0 °C. Valuable insights were obtained regarding the residual structure in cold unfolded states as well as the associated cooperativity of unfolding. However, the molecular cores of these model proteins do not contain any buried sidechain−sidechain H-bond (only the cores of frataxin and IscU contain each a single sidechain—backbone H-bond), while the polar moieties forming sidechain−sidechain H-bonds can be expected to be best suited to optimally coordinate individual water molecules in the core. Because of this, these model proteins are ill suited as starting points to efficiently test hypotheses regarding the "competition" of the two types of ordered water molecules for the formation of cold unfolded state structures and associated unfolding cooperativity.

To create a versatile platform to systematically test hypotheses related to protein cold unfolding, we turned to protein design.[48] We redesigned a previous protein design target, that is, the hyperthermostable 13 kDa 4-helix bundle "DRNN" (ΔG° of unfolding ∼16 kcal·mol^{-1} at 25 °C; heat denaturation temperature >100 °C) which contains a de novo designed, entirely hydrophobic core.[49] Using a recently developed ROSETTA-based protocol,[50] we placed hydrophilic hydrogen bond (H-bond) networks within the core of DRNN. Experimental screening of designs lead to the identification of the 12 kDa Designed Cold Unfolding 4-helix bundle "DCUB1", which features a bipartite core with an H-bond network located at the center (and orthogonal to the main bundle axis) of the otherwise entirely hydrophobic core (Figures 2 and 3). Importantly, an NMR structure and corresponding multidimensional NMR data are available for DRNN (PDB ID: 2LCH),[49] and the surfaces of DRNN and DCUB1 are virtually identical because only core residues were changed for the redesign.

In stark contrast to DRNN, the folded state of DCUB1 is only marginally stable (ΔG° of unfolding ∼3 kcal·mol^{-1} at 25 °C), and cold and heat unfolding transitions are registered at −5 and 65 °C, respectively. Here, we present a comprehensive biophysical characterization of the cold unfolded, folded, and heat unfolded states of DCUB1 (and selected mutants) along with the respective unfolding transitions by using cryo-X-ray crystallography, NMR, circular dichroism (CD) and fluorescence spectroscopy, differential scanning calorimetry (DSC), small-angle X-ray scattering (SAXS), and molecular dynamics (MD) simulations.

This approach enabled a detailed structural and thermodynamic characterization of DCUB1 unfolding and the development of general hypotheses regarding protein cold unfolding and the associated degree of transition cooperativity. The new insights presented here are of high relevance for establishing a predictive theory of cold unfolding and cold alternate conformations to also enhance our general understanding of psychrophilic proteins and their function,[51] for improving protein design methodology,[52] and for the continuing "cold revolution" in biotechnology,[53] that is, the creation of a novel cold-active enzyme and ice-binding proteins.

METHODS

Computational Design. DCUB1 was designed using an earlier version of the Rosetta protocol developed for creating buried hydrogen bond networks in proteins.[50] First, the core of DRNN was defined as all residues with more than 18 neighbors, where two residues are a neighbor if their C^{α} atoms are within 10 Å. For all core residues, a fixed backbone design simulation with Monte Carlo sampling was performed[54] with the energy function modified[55] to only score steric repulsion ("fa_rep" = 0.44) and sidechain hydrogen bonding ("hbond_sc" = 1.1). During the Monte Carlo trajectory, after every Monte Carlo accept (i.e., after a rotamer change or amino acid change), the structure was analyzed to determine if

https://doi.org/10.1021/acs.jpcb.1c10750
J. Phys. Chem. B 2022, 126, 1212−1231

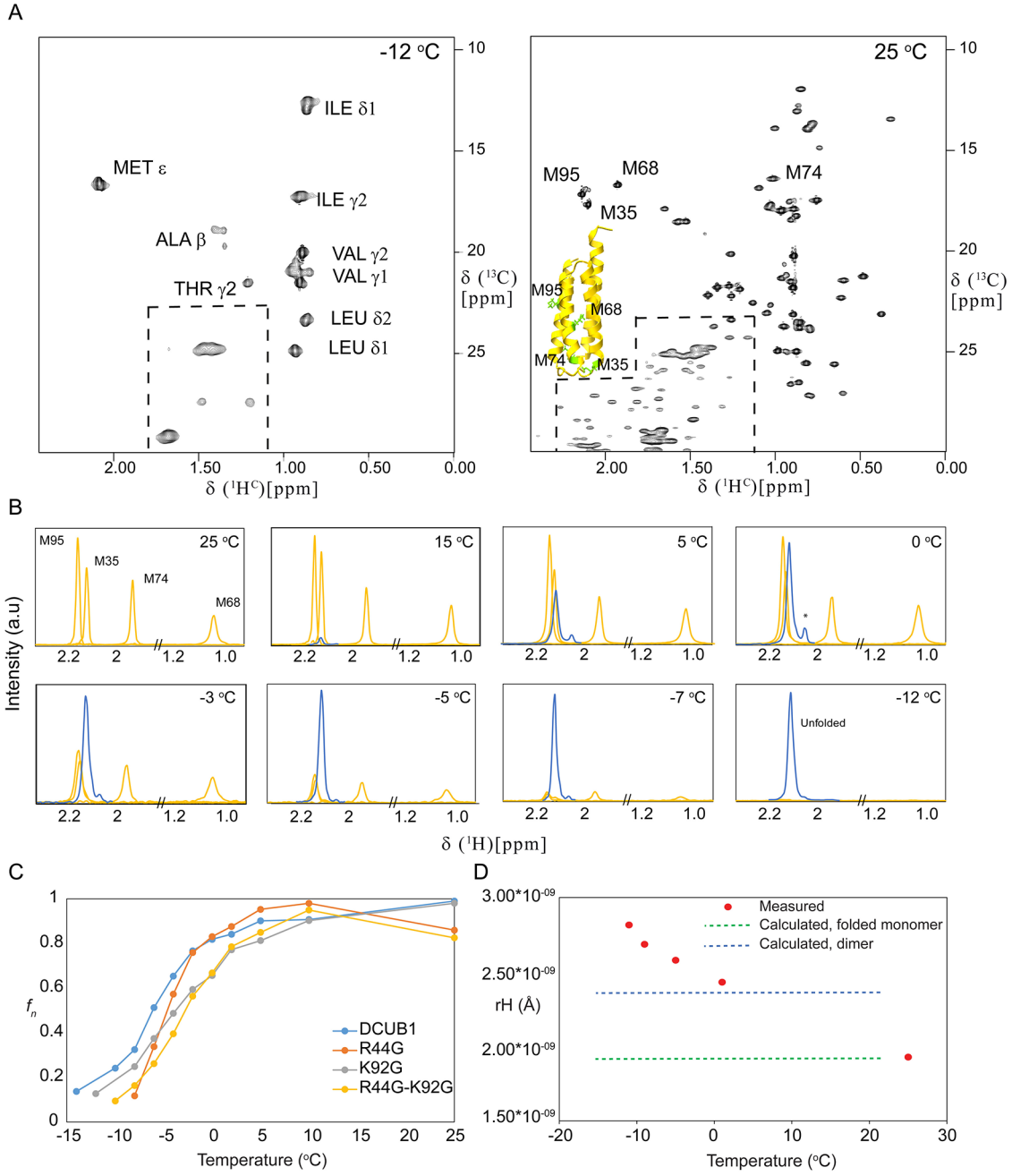

Figure 4. DCUB1 cold core unfolding (A to C) and cold dimer formation (D) monitored by NMR. (A) Methyl regions of the 2D [^{13}C,^{1}H]-COSY spectra recorded at −12 (on the left) and 25 °C (on the right). At −12 °C, a single peak cluster is observed at the random coil chemical shifts for each type of a methyl group which is indicated. At 25 °C, the resonance assignments of the four Met residues chosen for (B) are indicated and the ribbon drawing shows the location of these residues in the bundle. Signals in the boxes are from methylene groups. (B) $\omega_1(^1H^{methyl})$-slices taken from the 2D [^{13}C,^{1}H]-COSY spectra (Table S5.1) recorded between 25 and −12 °C (Figure S5.1). The folded state gives rise to four signals for the Met residues. The cold core-unfolded state giving rise to one major signal and a minor signal, indicating the presence of a lowly populated (<5%) cold core unfolding intermediate (labeled with an asterisk in the 0 °C cross section). (C) Fractions of folded state, f_n, vs T measured with 1D ^{1}H NMR for DCUB1, and mutants R44G, K92G, and R44G/K92G. The fractions for DCUB1 are very similar to the ratios of the integrals obtained for the signals of folded and unfolded state in (B). (D) Radius of hydration, r_H, of DCUB1 measured with 1D ^{1}H DOSY NMR vs T (Table S5.2, Figure S5.12). The radii calculated (Section S5 of the Supporting Information) for the folded state and a dimer are indicated as horizontal dashed lines. The data validate the SAXS-detected cold dimer formation (Figure 7D).

a new hydrogen bond network was present. A network being defined as a set of residues where each residue in the network is hydrogen bonding with another residue in the network and there exists a hydrogen bonding path between all residues in the network. At the end of the trajectory, the networks observed during the simulation were ranked by the number of residue pairs forming hydrogen bonds with each other. We visually inspected the top ranked designs and submitted about 10 to FastDesign simulations,[52] in which the rotamers of the hydrogen bonding residues were fixed but neighboring residues were allowed to mutate and the backbone was allowed to make small adjustments. The final designs were ranked by the

https://doi.org/10.1021/acs.jpcb.1c10750
J. Phys. Chem. B 2022, 126, 1212−1231

Table 1. Thermodynamic Parameters Obtained from Global Gibbs−Helmholtz Analyses[a]

	$T_{c,gGH}$	ΔH^o ($T_{c,gGH}$)	ΔS^o ($T_{c,gGH}$)	$T_{ms,gGH}$	ΔG^o ($T_{ms,gGH}$)	ΔH^o ($T_{ms,gGH}$)
DCUB1	-14 ± 0.2	-42 ± 1.1	-162 ± 8	27 ± 0.2	3.2 ± 0.14	3.2
R44G	-11 ± 0.7	-33 ± 2.9	-128 ± 19	24 ± 0.7	2.2 ± 0.20	2.2
K92G	-16 ± 0.3	-34 ± 1.4	-170 ± 8	23 ± 0.3	2.5 ± 0.16	2.5
R44G/K92G	-9 ± 0.7	-30 ± 2.6	-115 ± 17	23 ± 0.7	1.8 ± 0.16	1.8

	$T_{h,gGH}$	ΔH^o ($T_{h,gGH}$)	ΔS^o ($T_{h,gGH}$)	$\Delta C_{p,gGH}{}^o$	m	Integral ΔG^o dome	R^2
DCUB1	70 ± 0.2	51 ± 1.1	147 ± 3	1.10 ± 0.02 (1.14)	1.54 ± 0.02	182	0.997
R44G	61 ± 0.7	39.3 ± 2.9	117 ± 37	1.00 ± 0.08 (1.16)	1.15 ± 0.05	107	0.982
K92G	64 ± 0.3	41 ± 1.4	130 ± 3	0.93 ± 0.035 (1.15)	1.6 ± 0.04	137	0.996
R44G/K92G	57 ± 0.7	35 ± 2.6	107 ± 4	0.99 ± 0.072 (1.15)	1.44 ± 0.06	81	0.993

[a] T is in °C; ΔH^o in kcal mol^{-1}; ΔG^o in kcal mol^{-1}; ΔS^o in cal·mol^{-1}·K^{-1}; $\Delta C_{p,gGH}{}^o$ in kcal mol^{-1} K^{-1} with the predicted[56] values in parenthesis; m in kcal·mol^{-1}·M^{-1}; integral in kcal·K·mol^{-1}; R^2 represents the fraction of the variation of the response that is predicted by the model in the program Mathematica.

"Talaris" full atom energy function in Rosetta,[56] visually inspected, and DCUB1 was selected for experimental characterization. For details, see Supporting Information, Section S1.

MD Simulations. MD simulations (Table S2.1) were performed with established protocols using the program GROMACS[57] v5.1.3 with the AMBER99SB-ILDN force field, the TIP4P-Ew water model and chloride or Na ions, a box size of approximately 8 × 8 × 8 nm, periodic boundaries, and 2 fs step-size on GPUs of the XSEDE Comet cluster. The TIP4P-Ew model has been shown[58] to appropriately reproduce supercooled water properties and the closely related TIP4P/2005 water model has been successfully used for protein cold denaturation simulations.[59] Simulation systems were adjusted to 298 K during a 1 ns simulation with position restraints (*NVT* ensemble) using the V-rescale thermostat.[60] Prior to "production runs", the systems were equilibrated for 5 ns (*NPT* ensemble) at 1 bar pressure using the Parrinello−Rahman barostat.[61] MD simulations (Table S2.1; 130−600 ns each; total ∼4 μs) started from several different DCUB1 conformers: the Rosetta design model, the two X-ray structures of the asymmetric unit (chain-A with and without the water molecule in the H-bond network; chain-B with and without the water molecule in the H-bond network), the lowest energy NMR conformer, and the three Gly-mutants of DCUB1 derived from either the DCUB1 ROSETTA design model or the chain-B X-ray structure. For comparison, MD simulations were performed for DCUB1 at −50 °C starting from the X-ray structure (chain-A) as well as for the "parent" design DRNN at 25 °C starting from chain-B of the cryo-X-ray structure (PDB ID: 3U3B). MD trajectories were analyzed using the suite of programs in GROMACS[57] v5.1.3 and Visual MD (VMD).[62] For details, see Supporting Information, Section S2.

Protein Cloning, Expression, and Purification. Proteins were expressed with pCDB24 vectors as SUMO domain fusion proteins containing an N-terminal hexa-Histidine tag. The vectors were transformed into BL21(DE3) cells which were grown on MJ9 minimal media containing $^{15}NH_4Cl$ as the sole nitrogen source and *U*-^{13}C-glucose or 10% *U*-^{13}C-glucose/90% unlabeled glucose as the sole carbon source. The fusion proteins were purified using a Ni-NTA gravity column and cleaved by ULP1 SUMO protease. A second Ni-NTA chromatography step yielded the purified protein. To prepare high-quality mono-disperse SAXS samples, a gel-filtration step was added. For details, see Supporting Information, Section S3.

X-ray Crystallography. Crystallization of DCUB1 was performed using the same protocols used to crystallize DRNN.[49] Lyophilized DCUB1 was resuspended in water at 20 mg/mL and dialyzed into 100 mM ammonium acetate. Hanging drop vapor diffusion was used to grow crystals in 0.2 M magnesium acetate and 20% (w/v) PEG 3350. Crystals were cryo-protected by transferring them into a well solution supplemented with 15% (v/v) ethylene glycol before plunging into liquid nitrogen. Diffraction data were collected at 100 K at the Advanced Photon Source, Lemont IL. Crystals diffracted X-rays to a resolution of better than 1.4 Å in the *P*1 21 1 space group with cell parameters of a = 44.4 Å, b = 52.5 Å, c = 46.4 Å, α = 90.00°, β = 116.82°, and γ = 90.00° and contained two molecules in the asymmetric unit. The diffraction data were processed using HKL2000.[63] For details, see Supporting Information, Section S4.

Nuclear Magnetic Resonance Spectroscopy. For NMR data acquisition, samples of DCUB1 and the mutants R44G, K92G, and R44G/K92G were prepared in NMR buffer (50 mM Na phosphate, 100 mM NaCl, pH 7.0) at protein concentrations between 300 and 1.2 mM. 50 μM 4,4-dimethyl-4-silapentane-1-sulfonic acid (DSS) and an aliquot of complete protease inhibitor cocktail (Roche, Basel, Switzerland) were added to each sample. NMR data (Table S5.1) were acquired using an Agilent INOVA 750 MHz spectrometer equipped with a ^{1}H{^{13}C,^{15}N} probe and a Bruker AVANCE III HD 800 MHz spectrometer equipped with a cryogenic ^{1}H{^{13}C,^{15}N} probe. Temperatures were calibrated using a 99.8% deuterated methanol[64] sample. Chemical shifts were referenced to DSS. In

https://doi.org/10.1021/acs.jpcb.1c10750
J. Phys. Chem. B 2022, 126, 1212−1231

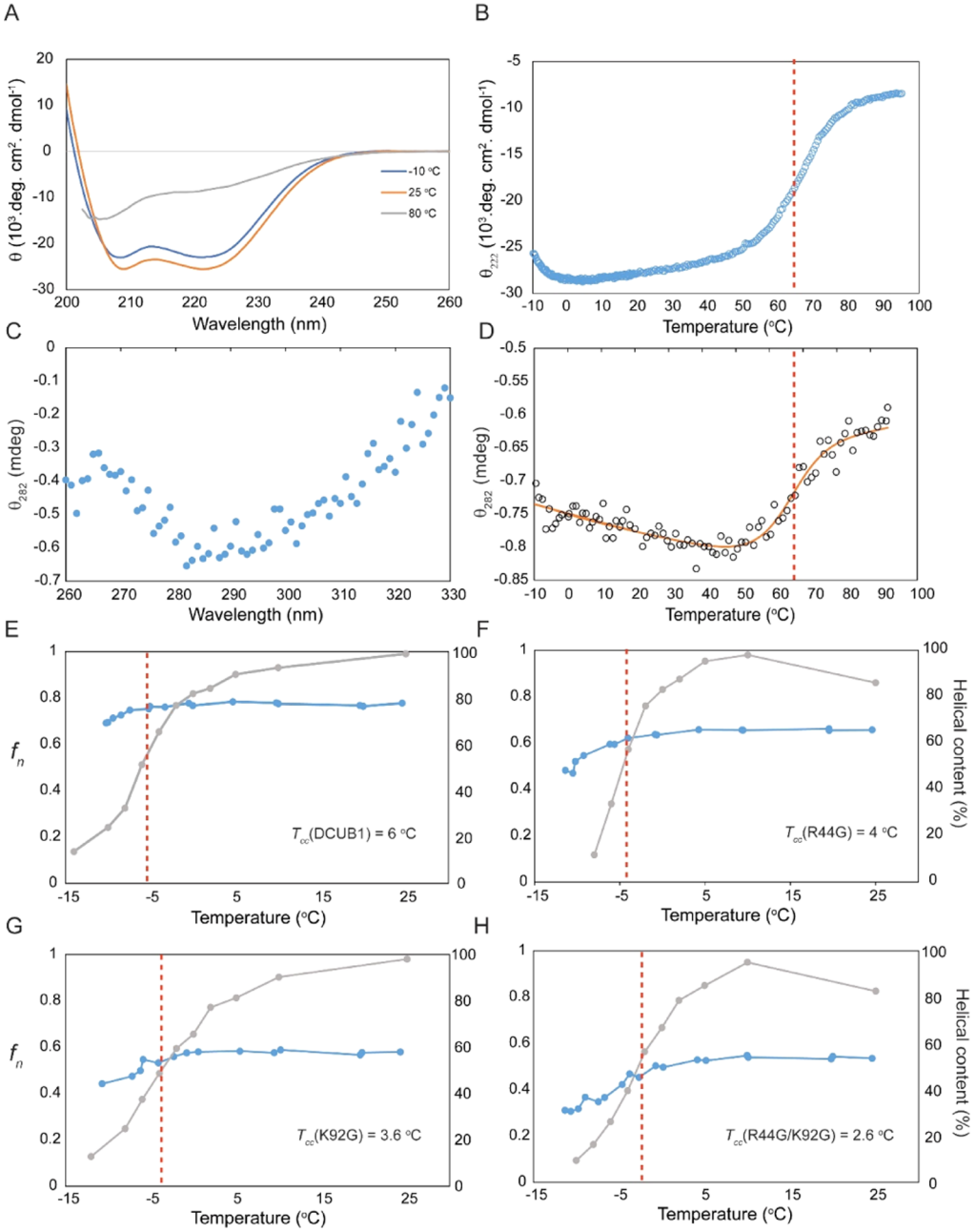

Figure 5. Discovery of cold helix unfolding decoupled from cold core unfolding, and heat unfolding monitored by CD (Figure S7.4). (A) Far UV CD spectra (all spectra are shown in Figure S7.2,7.3) recorded for DCUB1 at −10, 25, and 80 °C. (B) Far UV $\theta_{222}(T)$-profile recorded for DCUB1. The profiles for mutants R44G, K92G, and R44G/K92G are superimposed on this profile in Figure S7.4, and the van't Hoff analyses are shown in Figure S7.4C. (C) Near UV CD recorded for DCUB1 at 20 °C. (D) Near UV $\theta_{282}(T)$-profile recorded for DCUB1. (E) Helical content (blue dots; axis on the right) vs T for DCUB1 (Table S7.1). The gray dots represent the fractions of folded state vs T during cold core unfolding (Figure 4C) and $T_{cc,NMR}$ (Table 3) is indicated by a vertical dashed line. (F) Same as (E) but for R44G. (G) Same as (E) but for R92G. (H) Same as (E) but for R44G/K92G.

between measurements, samples were stored at −20 °C. For measurements below 0 °C, samples were prepared in thick-walled NMR tubes with an inner diameter of 3 mm (New Era, New York, NY), and samples were supercooled in the magnet by reducing T by about 0.1 °C/min.[35] To enable accurate quantitative analyses, all 800 MHz 1D ^{1}H and 2D COSY data were acquired with a 4 s relaxation delay between scans. Specifically, the fraction of the folded state, $f_n(T)$, was calculated as was described[34] from the total integral of two well resolved, upfield-shifted methyl signals of the folded state and an integral of aliphatic signals representing both folded and cold core-unfolded states in 1D ^{1}H NMR (Figures 4C and S5.4). Subsequently, we obtained from van't Hoff analyses for the cold core-unfolding transition $\Delta H_{cc,NMR}^{\circ}$ and $T_{cc,NMR}$. For details, see Supporting Information, Section S5.

Circular Dichroism Spectroscopy. Far UV CD $\theta_{222}(T)$ data for the global Gibbs−Helmholtz analysis of DCUB1 and the mutants R44G, K92G, and R44G/K92G (Table 1; Figure S7.1) were acquired between 4 and 97 °C on a Jasco J-815 CD spectrometer using a 1 mm cuvette at protein concentrations of 19 μM in NMR buffer (50 mM Na phosphate, 100 mM NaCl, pH 7.0). The same CD spectrometer was used to

https://doi.org/10.1021/acs.jpcb.1c10750
J. Phys. Chem. B 2022, 126, 1212−1231

acquire the near UV CD data for DCUB1 at 20 °C (Figure 5C) using a 1 mm cuvette at a protein concentration of 100 μM in NMR buffer. Far UV CD spectra (200−260 nm) for monitoring the helical content for DCUB1 and the mutants R44G, K92G, and R44G/K92G as a function of T (Figure S7.2; Table S7.1), and $\theta_{222}(T)$ to obtain melting temperatures and ΔH° values from van't Hoff analyses of unfolding transitions (Table 3) were acquired on a second Jasco J-815 spectrometer between −10 and 90 °C. This spectrometer is equipped with a multicell holder and data were acquired using a 1 mm cuvette at 10 μM protein concentration in NMR buffer (50 mM Na phosphate, 100 mM NaCl, pH 7.0). $\theta_{222}(T)$-profiles were fitted over the T-range of heat unfolding transition to the equation $\theta(T) = f_n\,\theta_n(T) + (1 - f_n)\,\theta_u(T)$, with $\theta_n(T)$ being a linear function of T and $\theta_u(T)$ being a quadratic function of T. Subsequently, van't Hoff analyses were performed using $K(T) = f_n(T)/[1 - f_n(T)]$ (Figure S7.3), yielding $\Delta H_{h,CD}^{\circ}$ and $T_{h,CD}$. For details, see Supporting Information, Section S7.

Fluorescence Spectroscopy. Fluorescence emission spectra were recorded for DCUB1 and the mutants R44G, K92G, and R44G/K92G between 0 and 95 °C on a Cary Eclipse spectrophotometer equipped with temperature controller (Varian Inc. Palo Alto, CA). Protein samples were prepared at ∼2 μM concentrations in a NMR buffer (50 mM Na phosphate, 100 mM NaCl, pH 7.0). The excitation wavelength was set to 295 nm and the emission spectra were recorded between 305 and 455 nm in 1 nm steps. Bandwidths for excitation and emission were set at 5 nm. Two observables were extracted from the spectra, that is, the total intensity TI (area under the emission spectrum) and the average emission wavelength, CM ("center of spectral mass"). With $X(T)$ = TI(T) (Figure S8.2) or CM(T) (Figure S8.3), T-profiles were fitted over the T-range of the heat unfolding transition to the equation $X(T) = f_n\,X_n(T) + (1 - f_n)\,X_u(T)$, with $X_n(T)$ and $X_u(T)$ being a linear function of T. Using $K(T) = f_n(T)/[1 - f_n(T)]$, linear van't Hoff fits were performed for the heat-unfolding transition to yield $\Delta H_{h,TIFL}^{\circ}$, $\Delta H_{h,CMFL}^{\circ}$, $T_{h,TIFL}$, and $T_{h,CMFL}$ (Table 3). For details, see Supporting Information, Section S8.

Small-Angle X-ray Scattering. Synchrotron SAXS data were collected at the BioSAXS beamline[65] 4−2 of the Stanford Synchrotron Radiation Lightsource (SSRL), Menlo Park, CA. The sample-to-detector distance was set to 1.7 m and X-rays of a wavelength of λ = 1.127 Å (11 keV) were used. Using a Pilatus3 X 1 M detector (Dectris Ltd, Switzerland), the setup covered the range of momentum transfer $q \approx 0.007-0.5$ Å^{-1} where q is the magnitude of the scattering vector defined as $q = 4\pi \sin\theta/\lambda$, with θ the scattering angle and λ the wavelength of the X-rays. Aliquots of 20−30 μL of sample solution was loaded into a capillary flow-cell, made from a standard X-ray quartz capillary (Hilgenberg GmbH, Germany) with a measured inner diameter of ∼1.3 mm and a nominal wall thickness of 0.01 mm. The temperature of the flow-cell was controlled using thermoelectric elements with an in-house built PID controller using an AD590 as a temperature transducer. The temperature scale of the setup was calibrated using a B&K precision thermometer (B&K Precision Corp, Yorba Linda, CA). A plastic tent was placed around the capillary holder and continuously flushed with dry nitrogen during the experiment (Figure S9.7) to eliminate condensation and eventual ice built up at temperatures below the hutch dew point (∼10 °C). The low-temperature limit for the experiment was established by visual observation of the sample in the capillary using the inline microscope at the beam line while reducing temperature and looking for initial ice formation. Data were collected at temperatures above this point. Data were collected at each temperature first from the buffer blank, followed by the protein sample and again another buffer blank to ensure proper cleaning of the capillary after the protein measurement. For the measurements below 0 °C, the samples were first loaded into the flow-cell at 0 °C and then cooled down to the target temperature. In order to ensure proper temperature equilibration, the sample was kept at the target temperature for about 5 min before measurements started. Series of ten to twenty 1 s exposures were collected and the sample solutions were oscillated in a stationary quartz capillary cell at 5 μL/s during data collection to maximize the exposed sample volume and thus to reduce the radiation dose per exposed sample volume. Due to the increase in viscosity of the sample with the decrease in temperature, the effective oscillation speed at low temperatures will be somewhat reduced; however, no significant increase in radiation sensitivity of the sample was observed. The collected data were radially integrated, analyzed for radiation damage by comparing the different frames with each series, and averaged and buffer subtracted using the automated data reduction pipeline SAXSPipe at the beam line. Subsequently, Guinier analysis, $P(r)$ function calculation, and molecular weight estimation were performed using programs from the ATSAS suite.[66] For details, see Supporting Information, Section S9.

Differential Scanning Calorimetry. DSC measurements were performed on a MicroCal Automated PEAQ-DSC instrument (Malvern Panalytical, Westborough, MA) for two identical DCUB1 DSC samples of 290 μM protein concentration (3.6 mg/mL) in NMR buffer (50 mM Na phosphate, 100 mM NaCl, pH 7.0) using published protocols.[67] Prior to sample analysis, the instrument performance was verified using the protocols described in the MCL2015 kit (Malvern Panalytical, Westborough, MA). The two DSC thermograms were acquired between 2 and 100 °C at a scan rate of 1 °C·min^{-1} and were fitted to a two-state model[67] using the MicroCal PEAQ-DSC software package. For details, see Supporting Information, Section S10.

RESULTS AND DISCUSSION

Computational Design. Designing hydrogen bond networks is a challenging problem because the vast majority of the buried polar groups need to have a hydrogen bond partner for the protein to have a favorable free energy of folding. To design a hydrogen bond network in the core of DRNN, we performed two rounds of simulations with the molecular modeling program Rosetta.[48] In the first round, the energy function was modified to only calculate the hydrogen bond energies and steric repulsion, and rotamer-based Monte Carlo optimization was used to find sets of amino acid sidechains that could form connected hydrogen bond networks. These sidechains were then fixed, and in the second stage of the protocol, the surrounding residues were redesigned to accommodate the new buried polar residues. A standard full atom energy function in Rosetta[56] was used for this stage. The resulting designs were ranked by the size of the hydrogen bond network and the calculated energy of the model. Our favorite design, named Designed Cold Unfolded Bundle 1 (DCUB1), was further characterized with 10 ns MD simulations at 25 °C to confirm that the designed hydrogen bond network remains

https://doi.org/10.1021/acs.jpcb.1c10750
J. Phys. Chem. B 2022, 126, 1212−1231

at least partially intact during the short simulations. DCUB1 contains 16 mutations relative to DRNN (Figures 2A and S1.1). In the design model, Asn 18, Asn 49, Glu 65, and Ser 97 are predicted to form a string of hydrogen bonds (Figure 3) stretching across the protein core from Asn 18 to Ser 97. Adjacent to this network, Ser 19 is also predicted to form a hydrogen bond to the wild type Thr 98. The other mutations in DCUB1 are substitutions to alternative hydrophobic residues.

Initial Assessment of Cold and Heat Unfolding. To assess if DCUB1 exhibits cold denaturation, we first performed an initial CD-based "global" Gibbs−Helmholtz (gGH) analysis[68] using guanidine hydrochloride (GHCl) as the chemical denaturant (Table 1; Figure S7.1). Importantly, GHCl was not used for any other study presented in this paper. Assuming that $\Delta C_{p,gGH}^{o}$ is constant, the global fit of $\theta_{222}[\Delta G^{o}(T), m{\cdot}c(\mathrm{GHCl}), T]$ predicted (i) cold/heat denaturation at $T_{c,gGH} = -14/T_{h,gGH} = 70$ °C, (ii) yielded $m = 1.54$ kcal·mol^{-2}, (iii) maximum stability at $T_{ms,gGH} = 27$ °C with $\Delta G^{o}(T_{ms}) = 3.2$ kcal·mol^{-1}, and (iv) $\Delta C_{p,gGH}^{o} = 1.10$ kcal·mol^{-1}·K^{-1} (1.13 kcal·mol^{-1}·K^{-1} is predicted using the equation of Spolar et al.[69]). Second, we acquired a series of 2D [^{15}N,^{1}H]-correlation spectroscopy (COSY) spectra of DCUB1 from 25 °C down to −12 °C in a supercooled solution (Figure S5.1,5.2). These spectra revealed the onset of cold unfolding around 10 °C, near completion of cold denaturation at −12 °C, and suggested that $T_c \sim -5$ °C is, in the absence of GHCl, somewhat higher. Two sets of signals were registered for the folded and the cold unfolded state showing that their interconversion is slow on the chemical shift timescale for all temperatures at or below 25 °C. An isotropic overall rotational correlation time of ∼7.5 ns was inferred from ^{15}N spin relaxation times (a hydrodynamic calculation[70] yielded 7.1 ns), showing that DCUB1 is monomeric in solution at 25 °C. Based on this initial assessment, DCUB1 was chosen for comprehensive biophysical characterization.

Folded State. An NMR solution structure of DCUB1 (PDB ID: 7T03) obtained at 25 °C (Table S5.2) and a 1.4 Å cryocrystallographic X-ray structure (PDB ID 7T2Y; Table S4.1) are very similar (Table 2; Figure 2). Both structures

Table 2. RMSD Values Calculated between DCUB1 X-ray and NMR Structures and the Rosetta Design Model

		backbone atom RMSD [Å]			
DCUB1		mean NMR coordinates	Rosetta model	X-ray chain-A	X-ray chain-B
heavy atom RMSD [Å]	mean NMR coordinates		0.62	0.74	0.76
	Rosetta model	1.19		0.51	0.49
	chain A	1.36	1.15		0.26
	chain B	1.50	1.40	1.14	

confirmed the accuracy of the Rosetta model (Figures 2 and S6.1,6.2): all pairwise RMSD values calculated for, respectively, backbone and all heavy atoms are in the ranges 0.51−0.74 and 1.14−1.50 Å (Table 2). A comparison of the design model with the experimental structures (Figure 2) revealed that the residues forming the two hydrophobic cores located above and below the H-bond network are in the designed χ^1 rotameric states (Figure S6.2). Intriguingly, however, the X-ray structures of both protein molecules in the asymmetric unit revealed a single tetra-coordinated water molecule within the H-bond network which forms H-bonds to the oxygen of the sidechain OH group of Ser 19, a proton of the sidechain NH_2-moiety of Asn 49, an oxygen of the sidechain CO_2-moiety of Glu 65, and the proton of the sidechain OH group of Ser 97 (Figure 3A,B). As a result, an unexpectedly complex hydrophilic network is formed in which three of the six H-bond residues (Asn 18, Ser 19, Asn 49, Glu 65, Ser 97, and Thr 98) are in different conformations when compared with the design model. First, the sidechain of Ser 19 forms (in both protein molecules of the asymmetric unit) a bifurcated H-bond to the water and the backbone carboxyl group of Leu 15 instead of the sidechain hydroxyl oxygen of Thr 98 in the design model. Second, the sidechain of Glu 65 adopts two alternate, about equally populated conformations (in both protein molecules in the asymmetric unit; Figure S4.1): one in which the CO_2-moiety forms a bifurcated H-bond with the water and the sidechain NH_2-moiety of Asn 49 and one in which it forms a bifurcated H-bond with the water and the sidechain OH-moiety of Ser 97. Third, the sidechain of Ser 97 adopts (in both protein molecules in the asymmetric unit) two alternate conformations, one in which the OH-moiety forms a bifurcated H-bond with the CO_2-moiety of Glu 65 and the internal water molecule and in which this moiety forms a H-bond with the backbone carboxyl group of Val 94. Moreover, additional H-bonds are observed in the X-ray structures (when compared with the design model), that is, (i) in both protein molecules of the asymmetric unit between the sidechain NH_2-moiety of Asn 49 and the backbone carboxyl moiety of Leu 15, and (ii) in one of the protein molecules of the asymmetric unit with two alternate conformations of the sidechain of Thr 98 between the OH-moiety of Thr 98 and the backbone carboxyl moiety of Asp 95 and in the other between this moiety and the backbone carbonyl of Val 94.

Comparison with the NMR structure shows, first, that the backbone dihedral angles (Figure S6.1) and nearly all sidechain χ^1-dihedral angles (Figure S6.2) observed in the X-ray structure are within the corresponding ranges of the 20 NMR conformers. Importantly, however, NMR showed that the entire H-bond network is subject to a pronounced slow conformational exchange at T_{ms}: the backbone NH signals of Ser 19 and Ser 97, the sidechain amide resonances of Asn 18 and Asn 49, as well as all sidechain resonances of Ser 19, Asn 49, Glu 65, Ser 97, and Thr 98 are severely broadened so that NOEs to their sidechains could not be detected [notably, the comparably high precision of the H-bond network observed in the NMR structure (Figure 2) results from steric constraints arising from its positioning between the two hydrophobic cores]. Hence, the X-ray H-bond network was "frozen out" in a low-energy configuration at ∼100 K. This view is supported by the fact that the B-factors of the internal water (as well as the other 282 water molecules) and the sidechains of the residues forming the network are not increased when compared with the remainder of the core. Furthermore, alternate conformations are observed for the sidechains of Glu 65, Ser 97, and Thr 98 (see above), and it may well be that the alternate X-ray conformations are the lowest-energy ones between which conformational exchange occurs at ambient T [such a correlation between the observation of alternate X-ray sidechain conformations and NMR line broadening was likewise observed for His 4 (backbone NH signal broadened) and Met 96 (backbone NH signals of Asp 95 and Met 96 broadened). Consistently, a comparative NMR structure calculation with constraints for sidechain−sidechain H-bonds

https://doi.org/10.1021/acs.jpcb.1c10750
J. Phys. Chem. B 2022, 126, 1212−1231

observed in the X-ray structure did not yield any NMR constraint violations and thus showed that the X-ray network structure is located entirely within the "allowed conformational space". Intriguingly, 13 methyl groups located in the two layers above and below the H-bond network (Figures 2 and S2.7) exhibit strong NOEs to water (Figure S5.9A). No such NOEs were observed for any of the methyl groups located further away from the network or for any of the methyl groups located in the core of DRNN.[49] Because the surfaces of DRNN and DCUB1 are virtually identical (only core residues were changed for redesign), NOEs mediated by rapidly exchanging protons on the surface would have also been detected for DRNN. Hence, we performed an NMR structure calculation for DCUB1 constraining a single water molecule with upper-limit distance constraints derived from the methyl−water NOEs. In the resulting NMR structure (Figure S5.9B), the water molecule is positioned very close to where it is detected in the X-ray structure (Figures 3 and S5.9C), while no violations of other NMR constraints were obtained. This finding strongly supports the notion that the water detected in the X-ray structure is likewise present as a long-lived water molecule at T_{ms} in solution.

MD simulations for DCUB1 at 25 °C (130−610 ns; total ∼2.7 μs) starting from four different conformers (i.e., design model, two X-ray structures in asymmetric unit, and the lowest-energy NMR conformer) showed that the core hydrogen bonds are highly populated and supported the notion that the water molecule in the network represents an integral structural feature (Figure 2; Supporting Information, Section S2). Remarkably, not a single exchange with a bulk water molecule was observed in our simulations (and in simulations started without the internal water molecule, it was accommodated in the network with the 2 ns equilibration period before the production run). This suggests that the lifetime of the molecule is ∼1 μs or longer. Considering also that methyl−water NOEs are measured at the chemical shift of bulk water (i.e., exchange is fast on the chemical shift time scale), we estimate that the lifetime is in the typically observed[71,72] range of about 1−100 μs. Moreover, in two of the simulations at 25 °C, as well as comparative 100 ns simulation at −50 °C, two additional water molecules were located above the H-bond network (Figure S2.8), suggesting that the onset of cold unfolding may be mediated by the intrusion of water molecules into (and above) the H-bond network. All simulations revealed consistently a pronounced gradient of internal core mobility from top (high mobility) to bottom (low mobility) in the orientation chosen for Figure 3 (Figure S2.7; Table S2.3,2.4), and backbone RMSD basin analyses showed that larger conformational excursions are associated with partial helix−coil transitions of helices I and IV (Figure S2.3−2.5). While simulations starting with the design model or an X-ray structure sample conformational space rather close to the starting structure (backbone heavy atom RMSD values remain <∼4 Å for simulations of comparable length; Table S2.2), simulations with the ambient temperature lowest-energy NMR conformer sample a significantly larger space (RMSD up to ∼6 Å; Table S2.2). This is consistent with the view that the X-ray structures represent low-energy conformers which are "frozen out" in the vitrified state at a cryogenic T of ∼100 K, while solution NMR structure constraints define "an allowed conformational space" which may include higher-energy conformers.

Rosetta Energies of Internal Water Molecules. The cryo-X-ray structure revealed that the internal water molecule is exceptionally well coordinated by the sidechains of the H-bond network (Figures 2 and 3), and it exhibits a B-factor which is well within the range of the protein heavy atom B-factors. Moreover, NMR revealed its presence at T_{ms} = 25 °C (Figure S5.9) and, in conjunction with MD, a lifetime in the range of ∼1−100 μs. We performed a Rosetta energy minimization of the two X-ray structures and the lowest energy NMR conformer containing internal water. The positions of the water molecules changed by less than ∼0.3−0.4 Å and the calculated energies for the waters were favorable between about 2 and 2.5 kcal·mol^{-1}. The same result was obtained for the first frames of the MD simulations started with the X-ray structure and the NMR structure. Hence, our Rosetta calculations strongly support the view that the internal water molecule is indeed in a LELS state.

We performed the same calculations for the first frame taken from the comparative simulation at −50 °C, in which two additional water molecules are located above the H-bond network (Figure S2.8). Intriguingly, one of the additional water molecules is located within the hydrophobic core above the H-bond network and yielded a positive Rosetta energy. Evidently, the energy minimization did not move this water into an energetically more favorable position, suggesting that such higher H internal water molecules may play an important role to nucleate the formation of energetically favorable networks of water molecules on hydrophobic surfaces.

Comparison of Molecular Cores of DCUB1 and Cold Unfolding Model Proteins. The bipartite hydrophilic−hydrophobic core of DCUB1 (Figures 2 and 3) represents a salient design feature, and the hydrophilic sidechain−sidechain interactions could be envisaged to function as a "sponge" to accommodate individual LELS water molecules without necessarily disrupting the polypeptide backbone conformation. To compare, we analyzed the cores of the five model proteins studied thus far, that is, 91-residue CTL9 (PDB ID: 1DIV; residues 58−149), 111-residue yeast frataxin yfh1 (2FQL), 126-residue apo-IscU (3LVL; Chain-B), dimeric 66-residue CylR2 (1UTX), and the 95-residue HIV-1 protease monomer 1−95 (5JFP; residues 1−95). Furthermore, we analyzed the core of 79-residue apoKti11[73] (5AX2) which cold unfolds above 0 °C and exhibits a rare hyperbolic $p-T$ phase diagram, but for which no detailed characterization of the cold unfolded state is available. Fully buried core residues were defined as having less than a 10% solvent accessible surface area. The analysis revealed that the cores of these six model proteins do not contain any buried hydrophilic sidechain−sidechain interactions, and solely the cores of frataxin and IscU contain a single hydrophilic sidechain−backbone H-bond each. Hence, the cores as well as the protein−protein interface of the CylR2 dimer are (nearly) entirely hydrophobic. This comparison underscores the importance of protein design for creating novel cold denaturing proteins to robustly test and validate theories explaining protein cold unfolding.

Cold Transitions and Cold States. *NMR Spectroscopy: Cold Unfolding of the Core.* To monitor polypeptide backbone and molecular core during cold unfolding, a series of 2D [^{15}N,^{1}H]- and [^{13}C^{methyl},^{1}H]-COSY spectra were recorded between T_{ms} = 25 and −12 °C in a supercooled solution (Figures 4 and S5.1,5.2; Table S5.1,5.2). Analysis of the 2D [^{13}C^{methyl},^{1}H]-COSY spectra revealed (i) that cold unfolding is entirely reversible, (ii) two distinct sets of signals

https://doi.org/10.1021/acs.jpcb.1c10750
J. Phys. Chem. B 2022, 126, 1212−1231

Table 3. Thermodynamic Parameters[a]

Cold core unfolding from NMR			
	$T_{cc,NMR}$ ± std dev	$\Delta H^{o}_{cc,NMR}(T_{cc,NMR})$ ± std dev	ΔS^{o} $(T_{cc,NMR})$ ± std dev
DCUB1	-6.0 ± 0.1	-43 ± 2.0	160 ± 8
R44G	-4.0 ± 0.4	-57 ± 6.4	212 ± 24
K92G	-3.6 ± 0.2	-31.9 ± 1	118 ± 4
R44G-K92G	-2.6 ± 0.1	-43.1 ± 1	159 ± 3
Heat unfolding			
θ_{222}-profile from CD			
	T_h ± std dev	ΔH^{o} (T_h) ± std dev	ΔS^{o} (T_h) ± std dev
DCUB1	$T_{h,CD}$ = 65 ± 0.02	$\Delta H^{o}_{h,CD}$ = 40 ± 0.5	118 ± 1.5
R44G	61 ± 0.03	41 ± 0.6	123 ± 1.7
K92G	59 ± 0.11	34 ± 3.8	103 ± 11.5
R44G-K92G	56 ± 0.01	35 ± 0.3	108 ± 0.9
Total intensity (*TI*) from fluorescence spectra			
DCUB1	$T_{h,TIFL}$ = 62 ± 0.4	$\Delta H^{o}_{h,TIFL}$ = 36 ± 1.7	108 ± 5.1
R44G	57 ± 0.3	35 ± 1.5	107 ± 4.4
K92G	57 ± 0.3	35 ± 1.6	106 ± 4.8
R44G-K92G	52 ± 0.4	31 ± 1.8	96 ± 5.4
Center of spectral mass (*CM*) from fluorescence spectra			
DCUB1	$T_{h,CMFL}$ = 68 ± 0.4	$\Delta H^{o}_{h,CMFL}$ = 35 ± 1.9	103 ± 5.6
R44G	64 ± 0.3	37 ± 2.1	108 ± 6.1
K92G	63 ± 0.1	38 ± 1.1	113 ± 3.2
R44G-K92G	59 ± 0.2	37 ± 1.6	111 ± 4.9
DSC			
	$T_{h,cal}$ ± std dev	ΔH^{o}_{cal} $(T_{h,cal})$ ± std dev	$\Delta C_p{}^{o}_{cal}$ $(T_{h,cal})$ ± std dev
DCUB1	61 ± 0.5	ΔH^{o}_{cal} = 39 ± 1.0	1.05 ± 0.05

[a] T is in °C; ΔH^{o} in kcal·mol^{-1}; ΔS^{o} in cal·mol^{-1}·K^{-1}. Except for DSC, standard deviations were obtained from linear van't Hoff analyses.

for folded and cold state are registered, with a minor Met methyl signal indicating the presence of a lowly populated (maximum around 0 °C with <5%; Figure 4B) cold unfolding intermediate, (iii) ^{1}H methyl shifts of the folded state do not reveal any significant conformational changes, and (iv) a cold unfolding midpoint around −5 °C. Hence, the cold unfolding transition detected by 2D NMR (Figure 4) proceeds largely in a cooperative manner and can be approximated well by a two-state model. Because the ^{1}H linewidths of all well resolved methyl signals of the folded state simply scale with the viscosity increase when lowering T, corresponding excess line broadening was estimated to be smaller than ∼5 Hz. This finding shows that the lifetimes of the two states are very long on the chemical shift time scale (i.e., at least ∼100 ms). Furthermore, the chemical shifts of all cold state methyl signals are nearly identical to the expected aqueous random-coil values so that a single peak cluster is observed for each type of the methyl group (Figure 4A). This observation shows that all methyl groups are hydrated and that the bipartite core disintegrates, thereby resulting in a "cold core-unfolded state" (Figure 1). As expected, 2D [^{15}N,^{1}H]- and [^{13}C^{methyl},^{1}H]-COSY spectra recorded for DRNN at −10 °C show that the protein fold is unchanged and that its core remains entirely intact (Figure S5.6).

Analysis of the 2D [^{15}N,^{1}H]-COSY spectra revealed (i) that the backbone and sidechain amide (NH) signals of the cold core-unfolded state exhibit a reduced backbone amide proton shift dispersion (∼2 ppm) which, however, is somewhat larger than expected for a random-coil (Figure S5.1), and (ii) that many of the resolved signals exhibit significant line broadening, indicating the presence of extensive slow conformational exchange of the backbone of the cold core-unfolded state on the μs−ms timescale (the line broadening prevented the measurement of ^{15}N spin relaxation parameters to characterize the internal dynamics of the cold core-unfolded state). Moreover, the measurement of the temperature coefficients of amide proton shifts of 54 well resolved 2D [^{15}N,^{1}H]-COSY signals of the cold core-unfolded state revealed 19 amide moieties (35% of the well resolved signals) with coefficients less negative than −5 ppb/K which is indicative of hydrogen bond formation.[74] This finding suggests that a significant fraction of the helices remain intact in the cold core-unfolded state.

In order to structurally characterize the cold core-unfolded state further, we acquired triple-resonance as well as 3D

https://doi.org/10.1021/acs.jpcb.1c10750
J. Phys. Chem. B 2022, 126, 1212−1231

NOESY NMR data at 0 °C (Table S5.1). At this temperature, ~70% folded and ~30% cold core-unfolded states are present, and the signals of the folded state may serve as a reference for the analysis of the core cold-unfolded state signals. First, no NOEs were detected for any of the aromatic rings and the methyl groups for the cold core-unfolded state, which provides a strong additional evidence for the disintegration of the core. Second, as expected from the analysis of 2D [^{15}N,^{1}H]-COSY, severe line broadening in the 3D spectra prevented resonance assignment. Notably, however, sequential NH-NH NOEs were detected for 36 out of 69 spin systems, which further supported the notion that a significant fraction of the helices remains intact upon cold core-unfolding.

The fraction of the folded core-unfolded state, f_n, was calculated as was described[34] from the total integral of two well resolved, upfield shifted methyl signals of the folded state and an integral of aliphatic signals representing both folded and cold core-unfolded state in 1D ^{1}H NMR (Figures 4C and S5.10). The thus-obtained f_n-values are consistent with values obtained by integrating the 2D [$^{13}C^{methyl}$,^{1}H]-COSY signals of Met and Ile, which give rise to two signal clusters being well resolved between folded and cold core-unfolded states (Figures 4A and S5.1). Subsequently, we obtained from a van't Hoff analysis for the cold core-unfolding transition $\Delta H_{cc,NMR}^{o} = -43$ kcal/mol and $T_{cc,NMR} = -6$ °C (Table 3; Figure S5.11).

Far-UV CD Spectroscopy: Helices Remain Largely Intact in the Cold Core-Unfolded State but Start to Cold Unfold below −5 °C. To monitor the helical content (Table S7.1) during cold unfolding, CD spectra (Figures 5A and S7.2) were recorded from 25 °C down to −10 °C in a supercooled solution and the T dependence of the $\theta_{222}(T)$ was monitored in between their acquisition (Figures 5B and S7.4). Deconvolution of the CD spectra using the BestSel server[75,76] revealed that the helical content (Figure 5; Table S7.1) remains constant between 25 °C (77% content; consistent with the folded state containing a structure-based content of 79%) and −5 °C (76%; ~50% cold core-unfolded state) before dropping somewhat to 70% at −10 °C. Hence, the CD data reveal (i) that the helices remain largely intact in the cold core-unfolded state as it is present at about −5 °C, which is consistent with previous studies showing that individual helices are increasingly stabilized when lowering T down to about 0 °C,[77,78] and (ii) the onset of cold helix unfolding significantly below $T_{cc,NMR} = -6$ °C. The presence of an isodichroic point at 204.5 nm (Figure S7.2) suggests that the cold helix unfolding transition may well proceed in a cooperative manner. The conformational preferences of cold unfolded helices present in supercooled water as well as the corresponding CD spectra are unknown, which prevents the determination of thermodynamic parameters for this cold transition. However, the comparison of the T-dependence of the helical content and the NMR-based f_n-values for cold core unfolding (Figure 5E) clearly shows that the cold helix unfolding occurs at significantly lower T than the cold core unfolding. Hence, these two cold transitions are largely decoupled. Considering that ΔC_p^{o} for helix heat denaturation is both small and negative,[78] cold unfolding of individual helices is not necessarily expected at such low T. The discovered cold helix unfolding strongly suggests that either the heat and cold unfolded states are thermodynamically distinctly different (which in turn would suggest that they are also structurally distinctly different) or that the onset of cold unfolding of helices of DCUB1 below about −5 °C is associated with the formation of a SAXS-detected, putatively water-mediated dimer (see below).

Finally, comparison with the $\theta_{222}(T)$ profiles obtained using GHCl for the global Gibbs−Helmholtz analysis shows that GHCl denatures the helices of the cold core-unfolded state (Figure S7.1). Specifically, at −10 °C and without GHCl, an MRE value of about −25,000 deg cm^2 dmol^{-1} is measured (Figure S7.4), while in the presence of 5.8 M GHCl, an MRE of 1530 deg cm^2 dmol^{-1} (very similar to the MRE expected for a disordered protein) is obtained at 2 °C (Figure S7.1). This finding underscores the importance to study cold unfolded states of proteins in the absence of any chemical denaturant.

Near-UV CD Spectroscopy: Residual Structure in the Cold Core-unfolded State. We recorded a near-UV CD spectrum at 20 °C (Figure 5C) and then monitored its maximum $\theta_{282}(T)$, which is dominated by the CD of Tyr and Trp residues,[79] between 25 and −10 °C (Figure 5D): only a rather moderate decrease of θ_{282} is measured in this T range. Although it is quite challenging to relate the tertiary structure and near-UV CD spectra,[80] the rather small change indicates the presence of significant residual structure[81] in the core cold-unfolded state.

Fluorescence Spectroscopy: Residual Structure in the Cold Core-Unfolded State. A series of emission spectra (305−455 nm; excitation at 295 nm) were acquired from 25 °C down to 0 °C (Figures 6 and S8.1). At 25 °C, the maximum of the emission spectrum, λ_{max}, of Trp 39 is located at 325 nm, which is well within the range typically observed for Trp residues located within a protein's core:[82] λ_{max} is blue-shifted relative to entirely solvent exposed Trp (Figure S8.4) and 3-methyl-indole,[82] which exhibit, respectively, very similar λ_{max} at 358 nm and 365 nm. Notably, λ_{max} of Trp dissolved in NMR buffer hardly changes between 0 and 90 °C (Figure S8.4). First, the total intensity (*TI*, area under the emission spectrum) decreases to about 70% when lowering T from 25 to 0 °C (Figure S8.2), which is indicative of increased dynamic quenching[83] due to the cold core-unfolding. Second, monitoring λ_{max}, did not reveal any red shift or change of the average emission wavelength (*CM*, "center of spectral mass") when lowering T to 0 °C (Figure S8.3). Consistent with the near-UV CD data, the virtual absence of a red shift thus indicates[84] that the indole moiety of Trp 39 remains at least partially buried upon cold core-unfolding.

SAXS: Formation of a Dimer below −5 °C. To characterize further the cold unfolding transitions inferred from NMR and CD spectroscopy, we acquired solution SAXS profiles (Table S9.1) for DCUB1, DRNN, and R44G/K92G in the temperature range from T = 23 °C down to −10 °C (−12.5 °C for DRNN) in supercooled NMR buffer (Table S9.1 and Figures 7 and S9.3−9.5).

Inspection of the Guinier plots of the DRNN profiles along with those obtained for a concentration series acquired at −5 °C did not reveal any indication of aggregation or increased intermolecular interactions at any of the temperatures (Figure S9.1). Moreover, the corresponding Kratky plots as well as the pair-distance distribution functions, $P(r)$, indicated that DRNN is, as expected, well folded over the entire T-range with the calculated molecular weight being consistently within 10% of the expected value of 13 kDa (Figure 7F). In contrast, the radius of gyration, R_g, increases moderately and, within the precision of the measurements, linearly from with $\Delta R_g/\Delta T$ = 0.025 Å/K, that is, from 16.7 to 17.7 Å when cooling the sample from 23 to −10 °C (Figure 7E).

https://doi.org/10.1021/acs.jpcb.1c10750
J. Phys. Chem. B 2022, 126, 1212−1231

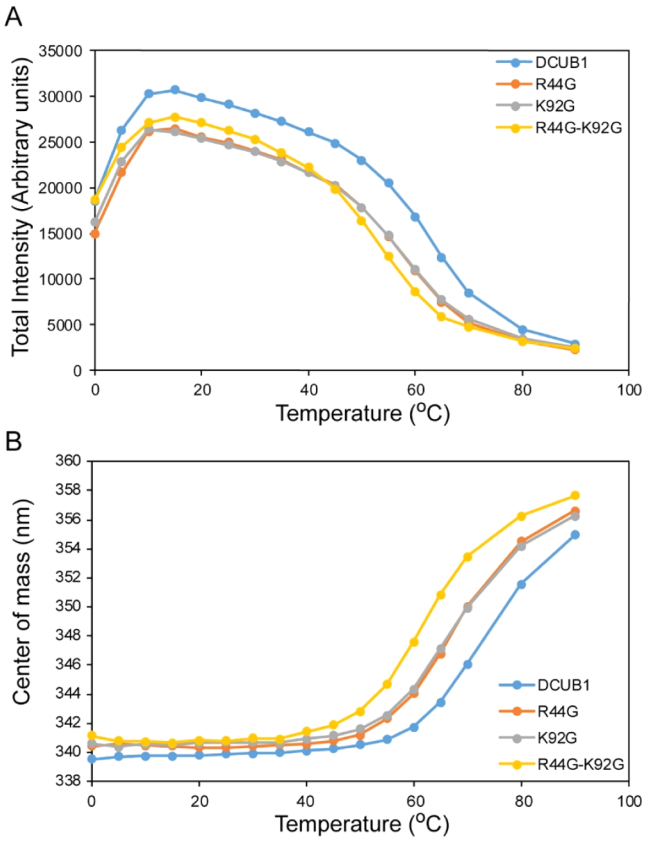

Figure 6. Onset of cold core unfolding and heat unfolding monitored by fluorescence spectroscopy (Figure S8.1) (A) TI(T)-profiles measured for DCUB1 and mutants R44G, K92G, and R44G/K92G. (B) CM(T)-profiles measured for the heat unfolding transitions of DCUB1 and mutants R44G, K92G, and R44G/K92G. Van't Hoff analyses of the heat unfolding transitions monitored in (A) and (B) yielded $\Delta H_{h,CMFL}^{\circ}$ and $T_{h,CMFL}$ (Table 3). The corresponding van't Hoff plots are shown in Figure S8.2,8.3, respectively.

A previous SAXS study of α_2-macroglobulin[85] revealed a moderate increase of scattering power when lowering T down to −15 °C and the authors suggested that this is due changes of core protein hydration. However, 2D [^{15}N,^{1}H]- and [$^{13}C^{methyl}$,^{1}H]-COSY spectra recorded for DRNN (Figure S5.6) showed that its core is not hydrated at −11 °C. Hence, the moderate increase of R_g upon supercooling likely results from a moderate and gradual expansion of the surface hydration of DRNN when lowering T.

For DCUB1, the inspection of the Guinier plots along with those obtained for a concentration series acquired at −5 °C also showed no significant aggregation at any of the temperatures (Figure 7A) and a SAXS profile acquired after cooling down to −12.5 and then returning to 23 °C was virtually identical to the initial one recorded at 23 °C, confirming that the cold transitions are entirely reversible. Standard Kratky plots (Figure 7B), Kratky plots normalized to the forward scattering intensity, I_0 (Figure S9.4), and P(r) functions (Figure 7C) reflect increasing structural disorder when lowering T from 23 to 10 °C. R_g remains nearly constant at ∼17 Å down to 0 °C (∼30% cold core-unfolded state), revealing that the cold core-unfolded state is rather compact at this T. The molecular weight inferred from the SAXS profiles remains within 10% of the value of DCUB1 (12.1 kDa) down to −0 °C. Intriguingly, however, the forward scattering intensity, I_0, is about 2.5-fold higher at −10 °C when compared with 25 °C (Figure 7A,D), R_g increases to ∼30 Å (Figure 7E), and the molecular weight doubles to about 25 kDa (Figure 7F).

Hence, the SAXS data acquired at −5 and −10 °C revealed the onset of an additional cold transition, that is, the formation of a cold dimer (Figure 1). Consistently, the maximum distance, D_{max}, of the $P(r)$ function approximately doubles, its maximum is shifted toward a higher r value (Figure 7C), and the Kratky plots (Figures 7B and S9.4) are indicative of a comparably ordered state. Because all methyl ^{1}H chemical shifts remain unchanged and at their respective random-coil values when lowering T from −5 to −10 °C (Figures 4A and S5.2), the methyl groups must remain fully hydrated upon dimerization. This can be explained by the formation of a "water-mediated dimer", possibly with a hydrated core resembling the one that was described for antifreeze protein Maxi.[86] The formation of such a dimer may well be driven by the formation of a larger number of LELS water molecules overcompensating the loss of entropy arising from dimerization (Figure 1). The moderate reduction of the helical content observed by CD when lowering T from −5 to −10 °C (Figure 5E) may indicate that some helical segments become disordered in the dimer.

Diffusion-ordered 1D ^{1}H NMR spectra[88] (DOSY) acquired between 25 and −11 °C (Figure S5.12) confirmed the cold dimer formation. At 25 °C, the hydrodynamic radius, r_H = 19.3 Å, is nearly identical to the value predicted by an X-ray structure-based hydrodynamic calculation[89] (19.6 Å; Figure 4C, Table S5.3). Upon cooling to −11 °C, r_H increases by about 50% to 28.2 Å and exceeds r_H = 24.2 Å which is predicted for a protein with twice the molecular weight of DCUB1 and the same axial ratio (1.98) when approximating the molecular shape as a prolate spheroid.[70] The SAXS data (Figures 7B and S9.4) showed that the cold dimer is compact but only partially folded. This provides a straightforward rationale[90] why the r_H value measured at −11 °C is about 20% in excess of the calculated value (notably, the cold dimer may also exhibit a larger axial ratio than the folded state which would contribute to the excess).

Heat Unfolding Transition and Heat Unfolded State. For a detailed understating of protein's (free) energy landscapes (Figure 1), it is important to compare cold and heat unfolding regarding (i) structural differences of cold and heat unfolded states, (ii) differences in cooperativity of cold and heat unfolding, and (iii) the thermodynamic equivalence of the two unfolded states. The latter point is related to the question if a single $\Delta G^{\circ}(T)$-dome suffices for an accurate thermodynamic description of both transitions. Hence, we employed DSC,[67] CD, fluorescence, and NMR spectroscopy to obtain complementary insights into the heat unfolding of DCUB1.

Differential Scanning Calorimetry. We measured the DSC[67] profile for DCUB1 between 2 and 95 °C (Figure 8), which yielded the calorimetrically measured heat unfolding temperature $T_{h,cal}$ = 61 °C, the enthalpy of unfolding, ΔH_{cal}° = 39 kcal/mol, and a heat capacity difference at $T_{h,cal}$ of ΔC_{pcal}° = 1.05 kcal·mol·K^{-1} (Table 3). The high quality of the fit for a two-state transition (Figure 8) and the observation that, within the experimental error, ΔH_{cal}° is equal to the van't Hoff values $\Delta H_{h,CD}^{\circ}$ and $\Delta H_{h,FL}^{\circ}$ (Table 3) show that heat unfolding does not involve intermediates which can be detected using DSC. Furthermore, the finding that, within the experimental error,

https://doi.org/10.1021/acs.jpcb.1c10750
J. Phys. Chem. B 2022, 126, 1212−1231

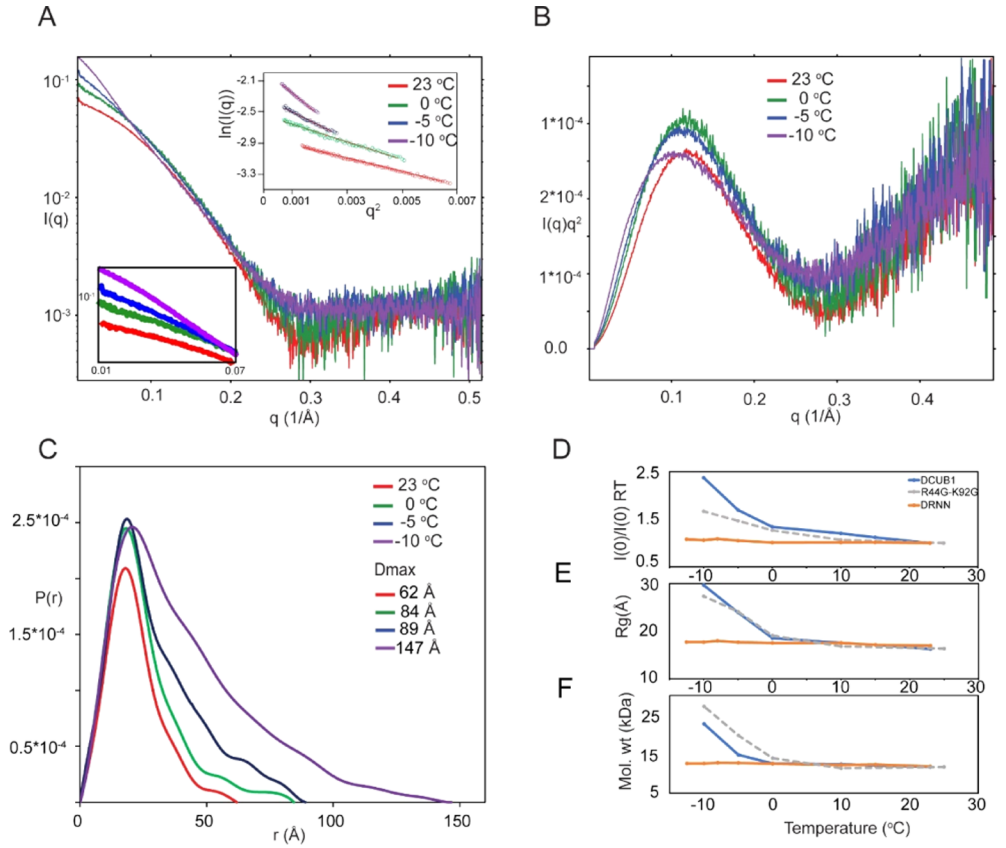

Figure 7. Cold dimer formation discovered by SAXS. (A) Log[$I(q)$] vs q plots for SAXS profiles recorded for DCUB1 at 23, 0, −5, and −10 °C. The low-q region is shown in the insert on the left, and the corresponding Guinier plots are shown in the insert on the right. (B) Kratky plots and (C) $P(r)$ functions for the SAXS profiles shown in (A). For proteins DCUB1, mutant R44G/R92G and DRNN are shown as follows: (D) I_0 normalized relative to I_0(23 °C) vs T, (E) R_g vs T, and (F) molecular weight derived from the volume of correlation[87] vs T.

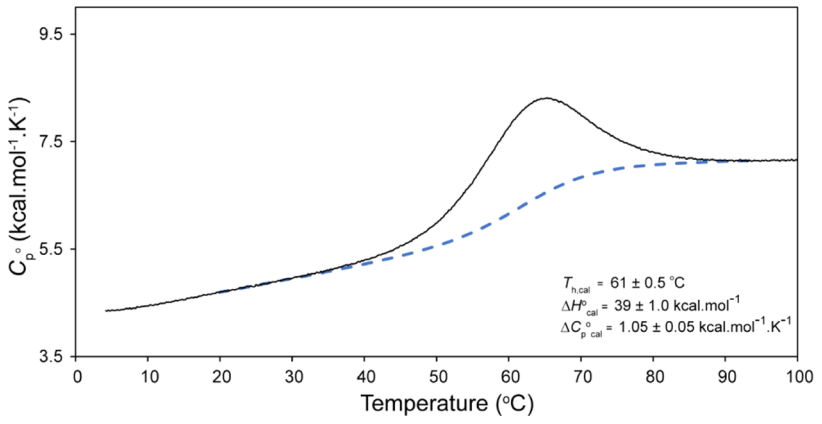

Figure 8. DCUB1 heat unfolding monitored by DSC. The partial molar heat capacity $C_{p,cal}^\circ$ vs T is shown as a solid line (the value for $C_{p,cal}^\circ$ for unfolded DCUB1 at T > 90 °C is in agreement with prediction[91]). The progress heat capacity[67] obtained from the fit of a two-state model is shown as a blue dashed line. The calorimetric thermodynamic parameters (Table 3) are indicated.

$\Delta C_{p,cal}^\circ = \Delta C_{p,gGH}^\circ$ indicates that the genuine heat unfolded state and the GHCl heat unfolded state are thermodynamically quite similar.

Far-UV CD Spectroscopy: Random-Coil Heat Unfolded State. To monitor the averaged helical content during the heat unfolding, a series of CD spectra were recorded from T_{ms} = 25−80 °C, and the T dependence of $\theta_{222}(T)$ was monitored in between their acquisition (Figures 5B and S7.3). The deconvolution of the CD spectra using the BestSel server[75,76] revealed that the helical content decreases from ∼77% at T_{ms} = 25 °C (consistent with the ∼95% folded state which contains a structure-based content of 79%) to ∼24% at 80 °C in the heat unfolded state (Table S7.1). Hence, the heat unfolded state features a helical content which is as expected for a random-coil according to the Bragg-Zimm theory[92] when considering the presence of helices I to IV comprising 25, 18, 15, and 17 residues, respectively. A van't Hoff analysis yielded $\Delta H_{h,CD}^\circ$ = 40 kcal·mol^{-1} and $T_{h,CD}$ = 65 °C (Table 3; we also performed a nonlinear fit of $\theta_{222}[\Delta G^\circ(T), T]$ using $\Delta C_{p,cal}^\circ$ = 1.05 kcal·

https://doi.org/10.1021/acs.jpcb.1c10750
J. Phys. Chem. B 2022, 126, 1212−1231

$mol^{-1}\cdot K^{-1}$ and virtually identical thermodynamic parameters were obtained).

Near-UV CD Spectroscopy: Increased Disorder in the Heat Unfolded State. Within the comparably low precision of the measurements, the $\theta_{282}(T)$ profile (Figure 5D) reflects the increased structural disorder arising from the transition of the folded state into a random coil.

NMR Spectroscopy: Random-Coil Heat Unfolded State. To monitor the polypeptide backbone during the heat denaturation transition, series of eight 2D [^{15}N,^{1}H]- and [$^{13}C^{methyl}$,^{1}H]-COSY spectra were recorded between T_{ms} = 25 and 60 °C (Figure S5.6,5.7). Considering that CD yielded $T_{h,CD}$ = 65 °C, about 50% of the protein is unfolded at 60 °C, and 2D spectra recorded after the sample was cooled back to 25 °C revealed that the heat denaturation is entirely reversible. Although accelerated amide proton exchange prevents recording of high-quality 2D [^{15}N,^{1}H]-COSY spectra above ∼50 °C, a largely reduced ^{15}N,^{1}H-chemical shift dispersion is observed at 60 °C for the heat unfolded state when compared to folded and cold core-unfolded states (Figure S5.1). Moreover, sharp methyl signals with chemical shifts close to their random-coil values are detected in 2D [$^{13}C^{methyl}$,^{1}H]-COSY spectra for the heat unfolded state at 60 °C (Figure S5.7), further supporting that the heat unfolded state results in a random coil.

Fluorescence Spectroscopy: Heat Unfolding Intermediate. A series of emission spectra (305−455 nm; excitation at 295 nm) were acquired between T_{ms} = 25 and 95 °C (Figure 6). First, the total intensity (*TI*, area under the emission spectrum) decreases by about 85% when increasing T to 90 °C. Second, in stark contrast to cold core unfolding, monitoring λ_{max} revealed a large red shift of 25 nm (to ∼350 nm at 95 °C), indicating that the indole moiety of Trp 39 is, in agreement with a random-coil state, largely solvent exposed in the heat unfolded state. Consistently, the average emission wavelength increases from ∼339 nm at 25 °C to ∼355 nm at 95 °C, and the average emission wavelength (*CM*, "center of spectral mass") increases accordingly. Van't Hoff analyses yielded for $\Delta H_{h,TIFL}^{\circ}$ = 36 $kcal\cdot mol^{-1}$, $\Delta H_{h,CMFL}^{\circ}$ = 35 $kcal\cdot mol^{-1}$, and $T_{h,TIFL}$ = 62 °C and $T_{h,CMFL}$ = 68 °C (Table 3; we also performed nonlinear fits using $\Delta C_{p,cal}^{\circ}$ = 1.05 $kcal\cdot mol^{-1}\cdot K^{-1}$ and virtually identical thermodynamic parameters were obtained). The two T_h values are very similar to the one obtained with CD, which indicates that increased dynamic quenching occurs along with the loss of helical content. However, the ∼6 °C difference between the two fluorometric T_h values indicates the presence of heat unfolding intermediates (Figure 1) in which the indole moiety of Trp 39 is, on average, located in less solvent exposed conformations as in the heat unfolded random coil.

Thermodynamic and Structural Hypotheses Tested with Mutants R44G, K92G, and R44G/K92G. It is well known that Gly residues destabilize helices[93−96] and thus α-helical proteins relative to their heat unfolded states. As a result, Gly mutations are expected to shift the $\Delta G^{\circ}(T)$-dome down to lower free energy values, which is associated with an increase of T_c and/or a decrease of T_h. Moreover, assuming that ΔC_p° is not significantly affected by the mutation, T_{ms} [$\Delta S^{\circ}(T_{ms})$ = 0 at this T] is expected to decrease. We studied the impact of Gly-mutations on cold core unfolding, helix cold melting, and cold dimer formation by creating variants of DCUB1 in which solvent-exposed helical residues, located at least two helical turns away from the H-bond network, are mutated to Gly (Figure S1.2). Specifically, we chose the mutants R44G (located in helix II comprising 20 residues) and K92G (in helix IV comprising 19 residues) as well as the double mutant R44G/R92G (Figure S1.2). 2D [^{15}N,^{1}H]-COSY (Figure S5.3−5.5) revealed that the mutants are well folded at T_{ms} and exhibit cold unfolding in the absence of GHCl around $T_{c,gGH}$ (Table 1). CD spectra recorded around T_{ms} revealed that the helical content in the folded state (Figure 5D−F) decreases according to DCUB1 (77%) > R44G (65%) > K92G (58%) > R44G/K92G (53%). MD simulations suggest that the low helical content of R44G/K92G results from enhanced partial helix−coil transitions in helices II and IV (Figure S2.6) arising from the mutations.

Initial assessment by CD-based global Gibbs−Helmholtz (gGH) analyses[68] using guanidine hydrochloride (GHCl) as the chemical denaturant largely confirmed the expected impact of the mutations on the $\Delta G^{\circ}(T)$-dome (Table 1): R44G, K92G, and R44G/K92G exhibit, respectively, $T_{c,gGH}$ = −11, −16, and −9 °C (DCUB1: −14), $T_{ms,gGH}$ = 24, 23, and 23 °C (DCUB1: 27) and $T_{h,gGH}$ = 61, 64, and 57 °C (DCUB1: 70), and $\Delta G^{\circ}(T_{ms})$ = 2.2, 2.5, and 1.8 $kcal\cdot mol^{-1}$ (DCUB1: 3.2). Consistently, the *m*-values are 1.15, 1.60, and 1.44 $kcal\cdot mol^{-1}\cdot M^{-1}$ (DCUB1: 1.54), respectively. It has recently been suggested[97] to calculate the integral Int[$\Delta G^{\circ}(T)$] (eq S1; positive area under the dome) between T_c and T_h to gauge the thermal stability, and we obtained Int[$\Delta G^{\circ}(T)$] = 107, 137, and 81 $kcal\cdot mol^{-1}\cdot K$ (DCUB1: 182). The $\Delta G^{\circ}(T_{ms,gGH})$ values and the integrals indicate that the impact of the two mutations is about additive. The $\Delta C_{p,gGH}^{\circ}$, values are, as predicted from sequence,[69] not significantly affected by the mutations, that is, 1.00, 0.93, and 0.99 $kcal\cdot K^{-1}\cdot mol^{-1}$ (DCUB1: 1.10). Subsequently, we acquired 1D ^{1}H NMR, CD, and fluorescence spectroscopic data as a function of T for all three mutants and SAXS profiles for R44G/K92G in order to assess the impact of the mutations on (i) cold core unfolding, (ii) cold helix unfolding, (iii) cold dimerization, and (iv) heat unfolding.

To study the cold core transitions of the mutants, a T-series of 1D ^{1}H NMR spectra (Table S5.1) was recorded to measure $f_n(T)$ (Figures 4C and 5F−H) and subsequent van't Hoff analyses yielded for R44G, K92G, and R44G/K92G, respectively, $T_{cc,NMR}$ = −4, −4, and −3 °C (DCUB1: −6) and $\Delta H_{cc,NMR}^{\circ}$ = −57, −32, and −43 $kcal\cdot mol^{-1}$ (DCUB1 = −43). The $T_{cc,NMR}$ values are only slightly increased (by about 2−3 °C), while the $\Delta H_{cc,NMR}^{\circ}$ values deviate somewhat from the value measured for DCUB1, with the values for R44G being more negative, the one for K92G being less negative, and the one for R44G/K92G being about the same. Hence, the impact of mutations on the thermodynamics of cold core unfolding is rather limited. This finding suggests that this transition depends largely on core stability and supports the view that it is largely driven by the formation of LELS water molecules around the core sidechains. Consistently, the fluorescence spectra of DCUB1 and all three mutants are very similar (Figures 6 and S8.1), that is, when lowering T from 25 to 0 °C, TI decreases to about 40%, which reflects similarly increased dynamic quenching due to the cold core-unfolding. Monitoring λ_{max} did not reveal any red shift or change of CM, which indicates that the indole moiety of Trp 39 in the mutants remain similarly buried upon cold core unfolding. Second, CD spectra (Figure S7.2) show that, as for DCUB1, the helical content (Table S7.1), albeit lower, remains nearly constant for all three mutants between 25 and −5 °C before dropping by ∼20% at −10°, and the presence of isodichroic points at the same wavelength of 204.5 nm (Figure

https://doi.org/10.1021/acs.jpcb.1c10750
J. Phys. Chem. B 2022, 126, 1212−1231

S7.2) suggest that the cold helix unfolding in the mutants may also proceed in a cooperative manner. The comparison of the T-dependence of the helical content and the NMR-based f_n-values for cold core unfolding (Figure 5F−H) shows that the cold helix unfolding also occurs at a significantly lower T than cold core unfolding. As for DCUB1, the CD data thus reveal (i) that the helices are as intact as in the folded state in the cold core-unfolded state at about −5 °C, and (ii) the onset of cold helix unfolding significantly below $T_{cc,NMR}$. Third, SAXS profiles acquired for R44G/K92G as a function of T (Figure S9.3−9.6) revealed that the cold dimer formation is not noticeably impacted by the mutations and is formed as for DCUB1. At 10 °C, R_g increases to about 28 Å (Figure 7E), which indicates comparable compactness, and the molecular weight is about doubled (Figure 7E).

To study the heat unfolding of the mutants, CD (Figure S7.3C−H) and fluorescence spectra (Figures 6 and S8.2,S8.3) were acquired. For R44G and R92G, the values for $T_{h,CD}$, $T_{h,TIFL}$, and $T_{h,CMFL}$ decrease by about ∼5 °C relative to the values measured for DCUB1 (Table 3 and Figures S8.2B and S8.3B). For R44G/R92G, the corresponding decreases are ∼10 °C. Hence, the mutations affect heat unfolding T_h values to a much larger extent than the cold core unfolding $T_{cc,NMR}$ values, and the impact of the mutations is about additive. All ΔH_h^o values are, within the experimental error, the same as the value obtained for DCUB1 (Table 3). About the same ∼6 °C difference is obtained between the two fluorometric T_h values, which indicates the presence of heat unfolding intermediates also in the mutants.

CONCLUSIONS

The present study illustrates that the computational protein design opens new avenues to study protein cold transitions and DCUB1 represents the first of a series of designs in our pipeline. In contrast to previously studied cold denaturing model proteins, DCUB1 contains a layered bipartite and a mixed hydrophilic/hydrophobic core featuring a H-bond network formed by several sidechains. Intriguingly, folded DCUB1 contains a tetra-coordinated, low-energy water molecule (lifetime in the μs range), which is not part of the computational design, in the H-bond network. When lowering T below T_{ms}, an unexpected and unprecedented complex set of cold transitions was discovered. First, below about 0 °C, the core of DCUB1 disintegrates and tertiary packing is lost, while a near-native helical content is retained. This finding was validated by studying Gly-mutants which exhibit quite similar cold core-unfolding T_{cc}. Moreover, the cold core-unfolded state exhibits a significant residual structure, which was also described for the four previously studied monomeric single-domain model proteins CTL9(L98A),[37,40−43] yeast frataxin yfh1,[18,38,44−46] 126-residue apo-IscU(D39A),[39] and HIV1 protease monomer.[47] Below about −5 °C, two additional cold transitions, which have not been described previously, are seen, that is, the formation of a water-mediated dimer and the onset of cold unfolding of helices, which is decoupled from the cold core unfolding. Gly mutations neither increased the temperature for the onset of helix unfolding nor impeded noticeably cold dimer formation. This suggests that such mutations either do not destabilize helices with respect to cold unfolding and/or that the helix cold unfolding is coupled to dimer formation. Currently, no theoretical approach[4,98] exists that predicts these experimental discoveries. Future studies are required to delineate a conformational ensemble representing the cold dimer which may inspire the engineering of new types of ice-binding proteins.[53]

Thus far, only the study of dimeric 66-residue CylR2,[36] revealed two different cold transitions, that is, the cold dissociation of the dimer followed by partial cold unfolding of the monomeric units, and it has been the only protein cold unfolding study in which cold transitions were structurally characterized at a higher resolution by NMR at temperatures well below 0 °C (i.e., in supercooled solution). Our study of DCUB1 is the first cold unfolding study combining NMR, SAXS, and CD spectroscopy performed with supercooled solutions. Hence, future studies on other systems with supercooled solutions[32] may also reveal more than one, and potentially coupled cold transitions.

DCUB1 cold core unfolding proceeds in a largely cooperative manner and is, as expected for a LELS state, associated with a negative ΔH^o and a positive ΔS^o. The negative ΔH^o is primarily due to the formation of additional water-protein H-bonds as well as water−water H-bond networks on exposed hydrophobic surfaces. The positive ΔS^o results from the partial immobilization of the water molecules involved in these two types of additional H-bonds. Upon heat denaturation, both tertiary as well as most secondary structure is lost, and the heat unfolded state represents a random coil. As expected for a HEHS state, heat unfolding is associated with a positive ΔH^o and a negative ΔS^o. Taken together, these findings can be concisely summarized in a schematic representation of the energy landscape of DCUB1 (Figure 1), which above −5 °C is dominated by three macrostates (cold core unfolded, folded, and heat unfolded), while at even lower T, the cold core-unfolded state forms a water-mediated dimer. Additional complexity is added by the onset of helix cold unfolding which is decoupled from the cold core unfolding.

In previous studies, a combined thermodynamic description of cold and heat unfolding relied on the Gibbs−Helmholtz (GH) equation which is employed under the assumption that ΔC_p^o does not depend on T and is the same for the cold and the heat unfolding transition. This approach implies "thermodynamic equivalence" of cold and heat unfolded states and results in a well-known two-state $\Delta G^o(T)$ function with a dome-like shape and zero-crossings at both T_c and T_h. The importance of cold denaturation studies to (i) assess protein stability whenever heat denaturation is associated with aggregation (aggregation upon cooling is rare, likely because the dielectric constant of water increases[99] when lowing T), and (ii) accurately estimate a constant ΔC_p^o and thus the $\Delta G^o(T)$-dome has been emphasized. However, given the significant structural differences of the cold and heat unfolded states of DCUB1, it appears problematic to justify the assumption that ΔC_p^o is the same for both transitions. The same may hold for previously studied model proteins. Cold denaturation ΔC_p^o values have not yet been measured so that comparisons with the corresponding values for heat denaturation are not available. Hence, future studies will be necessary to reveal for which proteins this conjecture holds. In addition, our study confirms the importance of not using chemical denaturants: they denature the genuine cold unfolded state(s) and artifactually result in thermodynamically (nearly) equivalent chemically unfolded cold and heat unfolded states.

Because the interconversion of folded and cold core-unfolded states is slow ($<\sim 10\ s^{-1}$), a significant free energy barrier must exist for this cold transition. The same was

https://doi.org/10.1021/acs.jpcb.1c10750
J. Phys. Chem. B 2022, 126, 1212−1231

observed for the four monomeric single domain model proteins CTL9(L98A),[37,40−43] yeast frataxin yfh1,[18,38,44−46] apo-IscU(D39A),[39] and HIV1 protease monomer.[47] Further studies will be necessary to delineate the relative importance of entropy and energy changes associated with the formation of a transition state ensemble (TSE), but it can expected that the free energy barrier results from a complex interplay of entropic (primarily due to the increase in conformational entropy and the loss of entropy of bound water molecules) and enthalpic effects (primarily due to the loss of protein−protein H-bonds and the formation of new water-protein and water−water H-bonds).

Our study revealed that the H-bond network of DCUB1 readily accommodates an internal low-energy water molecule. First, considering that individual H-bonded core water molecules stabilize protein molecules by 0.6−4 kcal/mol,[71,72] while $\Delta G^{o}(T_{ms})$ = 3.2 kcal/mol for DCUB1, the water molecule detected in the H-bond network may well be critical for the foldedness of DCUB1 at T_{ms}. This view is supported by Rosetta calculations which showed that the water molecule is highly stabilized by favorable H-bond interactions within the buried polar H-bond network. Second, MD simulations suggest that the onset of cold core unfolding is mediated by the intrusion of water molecules into the hydrophilic part of its bipartite core. In particular, the insertion of water molecules in between more flexible hydrophilic sidechains, which does not disrupt secondary structure elements, appears to be crucial. Hence, the internal H-bond network might serve as a "predetermined breaking point" nucleating cold core unfolding. This view is supported by the detection of a lowly populated (<5%) cold core unfolding intermediate. For proteins with an entirely hydrophobic core, for example, frataxin, clusters of charged surface residues may act as a "preferential gate for the entrance of water molecules into the core".[100] Furthermore, water insertion may likewise stabilize the cold denaturation TSE, reduce the free energy barrier, and thus accelerate cold core unfolding. In this case, the presence of internal water molecules may point at hitherto unknown free energy relationships[101] connecting thermodynamics and kinetics of cold core unfolding. Similarly, the excessive NMR line broadening observed for the polypeptide backbone amide moieties of the cold core-unfolded state indicates that the water molecules enable fast interconversion between the conformers representing this state, pointing at their well-known role as a lubricant[15] for protein folding.

It is unknown which structural features determine the cooperativity of cold core unfolding. The formation of energetically favorable networks of water molecules on hydrophobic surfaces is inherently a cooperative process involving several water molecules. Consistently, the monomeric single domain model proteins CTL9(L98A),[37,40−43] yeast frataxin yfh1,[18,38,44−46] and HIV1 protease monomer,[47] all of which feature a core devoid of sidechain−sidechain hydrophilic interaction, have been shown to cold unfold (above 0 °C) cooperatively. In contrast, even a single water molecule can be ordered through multiple hydrophilic interactions with the protein, which has been observed in an MD simulation of the cold unfolding of the "Trp-cage miniprotein".[59] In fact, most water molecules located in protein cores are individual, located close to the protein surface and form 3.7−4.3 H-bonds[71] (some are bifurcated). Moreover, they are rare in α-helical proteins and are often coordinated by loops,[71] which supports the view that sidechains are required to optimally coordinate internal water. We hypothesize that the mechanism of cold core unfolding of DCUB1 results from the segmentation of the core into two hydrophobic and one hydrophilic segment: water penetrates first into the central H-bond network which is followed by the cooperative disintegration of the two small hydrophobic cores above and below the H-bond network. This mechanism offers an explanation for the largely cooperative cold core unfolding of DCUB1, which is remarkable given (i) that individual water molecules can be accommodated by the internal H-bond network and (ii) the rather low relative contact order[102] (∼0.075) of DCUB1.

It is widely acknowledged that the entire conformational space sampled by protein molecules in solution is intimately linked to their folding and function.[6,7,24,103] This evidently includes states which are lowly populated at ambient T at which the folded state dominates. Such states exhibit elevated free energies and may distinctly differ in structure when compared with the folded state typically captured in atomic resolution structures. Recognizing that both LELS and HEHS states are lowly populated at ambient T, it can be expected that both may be of biological importance. While the potential importance of cold unfolded states for folding has been recognized, most of the thus far reported structural characterizations of lowly populated states of biological importance assume that those are HEHS states. However, it is in many cases unclear if the experimental characterization of lowly populated states, primarily by NMR[24,29,104] and room T X-ray crystallography,[5] captures LELS or HEHS states. When referred to as "excited states", we surmise an interpretation bias which results from the vast number of heat unfolding studies thus far complemented only by comparatively few cold unfolding studies. Evidently, functional roles discussed for HEHS states can likewise be envisaged for LELS states (e.g., they may play a role to modulate allosteric interactions). Notably, it has been shown that intrinsically disordered proteins are less cold sensitive. In this case, natural evolution has apparently resulted in proteins whose function is not negatively impacted by cold denaturation. Moreover, our study pointed at the importance of internal water for cold denaturation and, remarkably, the location of some internal water molecules is evolutionarily conserved.[71] This can be related to their role to form functionally important LELS states. Specifically, this may, quite generally hold for the function of antifreeze proteins as was recently suggested.[86]

Successful computational protocols to support the iterative engineering of novel cold denaturing proteins hold significant promise. First, it would be important to be able to design proteins which either unfold cooperatively or non-cooperatively. Arguably, engineering cooperatively denaturing proteins is more straightforward: based on current knowledge and our results, cooperativity can be expected for hydrophobic or bipartite cores with a central hydrophilic segment representing a pre-determined breaking point, and tuning of $\Delta H^{o}(T_{c})$ can adjust the steepness of the transition. In contrast, we hypothesize that proteins with a largely hydrophilic core, which enable the gradual insertion of water in the core associated with the formation of a quasi-continuum of partially unfolded macrostates, tend to cold denature non-cooperatively. This view is supported by the discovery of a lowly populated cold core-unfolding intermediate for DCUB1 which contains only a single internal H-bond network. Non-cooperatively cold unfolding proteins could potentially function as rheostats[23]

https://doi.org/10.1021/acs.jpcb.1c10750
J. Phys. Chem. B 2022, 126, 1212−1231

sensing T over a broad range. It can also be expected that future efforts to design cold unfolding proteins will improve the required computational protocols. For example, our failed attempt to computationally design cold denaturing "over-packed bundles", in which increased van der Waals repulsions destabilize the core, resulted in an important improvement of a central design protocol[52] used by the Rosetta community. Further improvements may include the involvement of explicit water molecules in the computational design and/or a suitable combination with explicit[14,18,105] or implicit[106] solvent MD simulations, which may also predict effects arising from variations of the ionic strength.[46]

Finally, new insights into cold transitions and the future development of theory to predict energy landscape and structural features of LELS states promise to (i) enhance our understanding of the role of cold transitions in biomedical research, for example, for amyloid fibril homeostasis[107] or vaccine development,[108,109] (ii) provide new insights into the functioning of psychrophilic proteins,[110] and (iii) support the engineering of cold-adapted enzymes and ice-binding proteins.[53] The use of protein design has proven to be a significant, efficient, and effective means to enhance our understanding of protein cold transitions.

■ ASSOCIATED CONTENT

Supporting Information

The Supporting Information is available free of charge at https://pubs.acs.org/doi/10.1021/acs.jpcb.1c10750.

> Comparison of DCUB1 and Rosetta design models; detailed analysis of MD trajectories; details of protein expression and purification; DCUB1 X-ray diffraction data collection and refinement statistics; electron density map of the H-bond network in DCUB1; NMR data acquisition parameters; plots of 1D and 2D NMR spectra; statistics of the DCUB1 NMR structure; NMR structure of DCUB1 derived with methyl−water NOES; van't Hoff analysis of DCUB1 cold core unfolding; details of analysis of DOSY spectra; comparison of DCUB1 design model with experimental structures; plots of CD spectra, their van't Hoff analysis, and helical content derived from CD spectra; fluorescence spectra and their van't Hoff analysis; SAXS data acquisition and analysis; plots of SAXS profiles, Kratky plots, T-dependence of R_g, and molecular weights; experimental setup for SAXS data acquisition in a supercooled buffer; and details of DSC data analysis (PDF)

Accession Codes

The X-ray and NMR structure of DCUB1 are deposited in the Protein Data Bank with accession codes 7T2Y and 7T03, respectively. The chemical shifts of DCUB1 are deposited in the Biological Magnetic Resonance Data Bank with accession code 30970.

■ AUTHOR INFORMATION

Corresponding Author

Thomas Szyperski − *Department of Chemistry, University at Buffalo, The State University of New York, Buffalo, New York 14260, United States;* orcid.org/0000-0003-0272-1373; Email: szypersk@buffalo.edu

Authors

Surya V. S. R. K. Pulavarti − *Department of Chemistry, University at Buffalo, The State University of New York, Buffalo, New York 14260, United States*

Jack B. Maguire − *Department of Biochemistry and Biophysics, University of North Carolina at Chapel Hill, Chapel Hill, North Carolina 27599, United States;* Present Address: Menten AI Inc., Palo Alto, California 94303, USA

Shirley Yuen − *Department of Chemistry, University at Buffalo, The State University of New York, Buffalo, New York 14260, United States;* Present Address: 73 Callodine Ave, Buffalo, NY 14226, USA.

Joseph S. Harrison − *Department of Biochemistry and Biophysics, University of North Carolina at Chapel Hill, Chapel Hill, North Carolina 27599, United States;* Present Address: Department of Chemistry, University of the Pacific, Stockton, California 95211, USA.

Jermel Griffin − *Department of Chemistry, University at Buffalo, The State University of New York, Buffalo, New York 14260, United States;* Present Address: Astrix Software Technology Inc, Red Bank, New Jersey 07701, USA.

Lakshmanane Premkumar − *Department of Microbiology and Immunology, University of North Carolina at Chapel Hill, Chapel Hill, North Carolina 27599, United States*

Edward A. Esposito − *Malvern Panalytical Inc, Northhampton, Massachsetts 01060, United States*

George I. Makhatadze − *Department of Biological Sciences, Rensselaer Polytechnic Institute, Troy, New York 08544, United States;* orcid.org/0000-0003-4565-1264

Angel E. Garcia − *Center for Non Linear Studies, Los Alamos National Laboratory, Los Alamos, New Mexico 87545, United States;* orcid.org/0000-0002-0912-0960

Thomas M. Weiss − *Stanford Synchrotron Radiation Lightsource, Stanford Linear Accelerator Center, Stanford University, Menlo Park, California 94025, United States*

Edward H. Snell − *Hauptman-Woodward Medical Research Institute, Buffalo, New York 14203, United States; Department of Materials Design and Innovation, University at Buffalo, The State University of New York, Buffalo, New York 14260, United States;* orcid.org/0000-0001-8714-3191

Brian Kuhlman − *Department of Biochemistry and Biophysics, University of North Carolina at Chapel Hill, Chapel Hill, North Carolina 27599, United States;* orcid.org/0000-0003-4907-9699

Complete contact information is available at: https://pubs.acs.org/10.1021/acs.jpcb.1c10750

Notes

The authors declare no competing financial interest.

■ ACKNOWLEDGMENTS

This work was supported by the National Science Foundation (MCB-1615570 to T.S. and B.K.; XSEDE MCB180104 to T.S.) and the National Institutes of Health (GM131923 to B.K.). A.E.G. was partially supported by Los Alamos National Laboratory LDRD program. Use of the Stanford Synchrotron Radiation Lightsource (SSRL), SLAC National Accelerator Laboratory, is supported by the U.S. Department of Energy (DE-AC02-76SF00515). The SSRL Structural Molecular Biology Program is supported by the DOE Office of Biological

and Environmental Research and by the National Institutes of Health (P30GM133894). The Pilatus detector at SSRL beamline 4-2 at SSRL was funded under National Institutes of Health (S10OD021512). NMR data were acquired at the SUNY ESF facility in Syracuse, NY, using an 800 MHz spectrometer funded by the National Institutes of Health (1S10OD012254). Computational support was provided by the Center for Computational Research at the University at Buffalo [http://hdl.handle.net/10477/79221]. J.G. was supported by a Ronald E. McNair fellowship. J.G. and S.Y. were supported by a scholarship of the Szyperski Foundation and as scholars of the BioXFEL STC (NSF award 1231306). We thank Dr. David Kiemle for support setting up the NMR experiments at the SUNY ESF facility, Drs. Victor Ovchinnikov and Aravinda Munasinghe for help to evaluate internal water residence times in our MD simulations, Dr. Van Ngo for helpful discussion regarding our MD simulations, and Dr. Catherine Royer for helpful discussions regarding the interpretation of fluorescence spectroscopic data.

REFERENCES

(1) Dill, K. A. Dominant Forces in Protein Folding. *Biochemistry* **1990**, *29*, 7133−7155.
(2) Kryshtafovych, A.; Schwede, T.; Topf, M.; Fidelis, K.; Moult, J. Critical Assessment of Methods of Protein Structure Prediction (CASP)—Round XIV. *Proteins: Struct., Funct., Bioinf.* **2021**, *89*, 1607−1617.
(3) Senior, A. W.; Evans, R.; Jumper, J.; Kirkpatrick, J.; Sifre, L.; Green, T.; Qin, C.; Žídek, A.; Nelson, A. W. R.; Bridgland, A.; Penedones, H.; Petersen, S.; Simonyan, K.; Crossan, S.; Kohli, P.; Jones, D. T.; Silver, D.; Kavukcuoglu, K.; Hassabis, D. Improved Protein Structure Prediction Using Potentials from Deep Learning. *Nature* **2020**, *577*, 706−710.
(4) Nassar, R.; Dignon, G. L.; Razban, R. M.; Dill, K. A. The Protein Folding Problem: The Role of Theory. *J. Mol. Biol.* **2021**, *433*, 167126.
(5) Fraser, J. S.; van den Bedem, H.; Samelson, A. J.; Lang, P. T.; Holton, J. M.; Echols, N.; Alber, T. Accessing Protein Conformational Ensembles Using Room-Temperature X-Ray Crystallography. *Proc. Natl. Acad. Sci. U.S.A.* **2011**, *108*, 16247−16252.
(6) Alderson, T. R.; Kay, L. E. Unveiling Invisible Protein States with NMR Spectroscopy. *Curr. Opin. Struct. Biol.* **2020**, *60*, 39−49.
(7) Dill, K. A.; Maccallum, J. L. The Protein-Folding Problem, 50 Years. *Science* **2012**, *338*, 1042−1046.
(8) Privalov, P. L. Cold Denaturation of Proteins. *Crit. Rev. Biochem. Mol. Biol.* **1990**, *25*, 281−306.
(9) Wolynes, P. G.; Onuchic, J. N.; Thirumalai, D. Navigating the Folding Routes. *Science* **1995**, *267*, 1619−1620.
(10) Karplus, M. Behind the Folding Funnel Diagram. *Nat. Chem. Biol.* **2011**, *7*, 401−404.
(11) Dias, C. L.; Ala-Nissila, T.; Wong-ekkabut, J.; Vattulainen, I.; Grant, M.; Karttunen, M. The Hydrophobic Effect and Its Role in Cold Denaturation. *Cryobiology* **2010**, *60*, 91−99.
(12) Ben-Naim, A. Theory of Cold Denaturation of Proteins. *Adv. Biol. Chem.* **2013**, *03*, 29−39.
(13) Mamontov, E.; Chu, X.-q. Water-Protein Dynamic Coupling and New Opportunities for Probing It at Low to Physiological Temperatures in Aqueous Solutions. *Phys. Chem. Chem. Phys.* **2012**, *14*, 11573−11588.
(14) Bellissent-Funel, M.-C.; Hassanali, A.; Havenith, M.; Henchman, R.; Pohl, P.; Sterpone, F.; Van Der Spoel, D.; Xu, Y.; Garcia, A. E. Water Determines the Structure and Dynamics of Proteins. *Chem. Rev.* **2016**, *116*, 7673−7697.
(15) Levy, Y.; Onuchic, J. N. Water Mediation in Protein Folding and Molecular Recognition. *Annu. Rev. Biophys. Biomol. Struct.* **2006**, *35*, 389−415.
(16) Davis, J. G.; Rankin, B. M.; Gierszal, K. P.; Ben-Amotz, D. On the Cooperative Formation of Non-Hydrogen-Bonded Water at Molecular Hydrophobic Interfaces. *Nat. Chem.* **2013**, *5*, 796−802.
(17) Baldwin, R. L. Dynamic Hydration Shell Restores Kauzmann's 1959 Explanation of How the Hydrophobic Factor Drives Protein Folding. *Proc. Natl. Acad. Sci. U.S.A.* **2014**, *111*, 13052−13056.
(18) Camilloni, C.; Bonetti, D.; Morrone, A.; Giri, R.; Dobson, C. M.; Brunori, M.; Gianni, S.; Vendruscolo, M. Towards a Structural Biology of the Hydrophobic Effect in Protein Folding. *Sci. Rep.* **2016**, *6*, 28285.
(19) Baldwin, R. L. The New View of Hydrophobic Free Energy. *FEBS Lett.* **2013**, *587*, 1062−1066.
(20) Durell, S. R.; Ben-Naim, A. Hydrophobic-Hydrophilic Forces in Protein Folding. *Biopolymers* **2017**, *107*, No. e23020.
(21) Roy, S.; Hecht, M. H. Cooperative Thermal Denaturation of Proteins Designed by Binary Patterning of Polar and Nonpolar Amino Acids. *Biochemistry* **2000**, *39*, 4603−4607.
(22) Malhotra, P.; Udgaonkar, J. B. How Cooperative Are Protein Folding and Unfolding Transitions? *Protein Sci.* **2016**, *25*, 1924−1941.
(23) Muñoz, V.; Campos, L. A.; Sadqi, M. Limited Cooperativity in Protein Folding. *Curr. Opin. Struct. Biol.* **2016**, *36*, 58−66.
(24) Mills, J. L.; Szyperski, T. Protein Dynamics in Supercooled Water: The Search for Slow Motional Modes. *J. Biomol. NMR* **2002**, *23*, 63−67.
(25) Korzhnev, D. M.; Salvatella, X.; Vendruscolo, M.; Di Nardo, A. A.; Davidson, A. R.; Dobson, C. M.; Kay, L. E. Low-Populated Folding Intermediates of Fyn SH3 Characterized by Relaxation Dispersion NMR. *Nature* **2004**, *430*, 586−590.
(26) Choy, W.-Y.; Zhou, Z.; Bai, Y.; Kay, L. E. An 15 N NMR Spin Relaxation Dispersion Study of the Folding of a Pair of Engineered Mutants of Apocytochrome b 562. *J. Am. Chem. Soc.* **2005**, *127*, 5066−5072.
(27) Korzhnev, D. M.; Neudecker, P.; Zarrine-Afsar, A.; Davidson, A. R.; Kay, L. E. Abp1p and Fyn SH3 Domains Fold through Similar Low-Populated Intermediate States. *Biochemistry* **2006**, *45*, 10175−10183.
(28) Pustovalova, Y.; Kukic, P.; Vendruscolo, M.; Korzhnev, D. M. Probing the Residual Structure of the Low Populated Denatured State of ADA2h under Folding Conditions by Relaxation Dispersion Nuclear Magnetic Resonance Spectroscopy. *Biochemistry* **2015**, *54*, 4611−4622.
(29) Zhuravleva, A.; Korzhnev, D. M.; Zhuravleva, A. Protein Folding by NMR. *Prog. Nucl. Magn. Reson. Spectrosc.* **2017**, *100*, 52−77.
(30) Hartl, F. U.; Hayer-Hartl, M. Converging Concepts of Protein Folding in Vitro and in Vivo. *Nat. Struct. Mol. Biol.* **2009**, *16*, 574−581.
(31) Poppe, L.; van Halbeck, H. NMR Spectroscopy of Hydroxyl Protons in Supercooled Carbohydrates. *Nat. Struct. Biol.* **1994**, *1*, 215−216.
(32) Skalicky, J. J.; Sukumaran, D. K.; Mills, J. L.; Szyperski, T. Toward Structural Biology in Supercooled Water. *J. Am. Chem. Soc.* **2000**, *122*, 3230−3231.
(33) Skalicky, J. J.; Mills, J. L.; Sharma, S.; Szyperski, T. Aromatic Ring-Flipping in Supercooled Water: Implications for NMR-Based Structural Biology of Proteins. *J. Am. Chem. Soc.* **2001**, *123*, 388−397.
(34) Szyperski, T.; Mills, J. L.; Perl, D.; Balbach, J. Combined NMR-Observation of Cold Denaturation in Supercooled Water and Heat Denaturation Enables Accurate Measurement of ΔCp of Protein Unfolding. *Eur. Biophys. J.* **2006**, *35*, 363−366.
(35) Szyperski, T.; Mills, J. L. NMR-Based Structural Biology of Proteins in Supercooled Water. *J. Struct. Funct. Genomics* **2011**, *12*, 1−7.
(36) Jaremko, M.; Jaremko, Ł.; Kim, H.-Y.; Cho, M.-K.; Schwieters, C. D.; Giller, K.; Becker, S.; Zweckstetter, M. Cold Denaturation of a Protein Dimer Monitored at Atomic Resolution. *Nat. Chem. Biol.* **2013**, *9*, 264−270.
(37) Li, Y.; Shan, B.; Raleigh, D. P. The Cold Denatured State Is Compact but Expands at Low Temperatures: Hydrodynamic

https://doi.org/10.1021/acs.jpcb.1c10750
J. Phys. Chem. B 2022, 126, 1212−1231

Properties of the Cold Denatured State of the C-Terminal Domain of L9. *J. Mol. Biol.* **2007**, *368*, 256−262.
(38) Pastore, A.; Martin, S. R.; Politou, A.; Kondapalli, K. C.; Stemmler, T.; Temussi, P. A. Unbiased Cold Denaturation: Low- and High-Temperature Unfolding of Yeast Frataxin under Physiological Conditions. *J. Am. Chem. Soc.* **2007**, *129*, 5374−5375.
(39) Bothe, J. R.; Tonelli, M.; Ali, I. K.; Dai, Z.; Frederick, R. O.; Westler, W. M.; Markley, J. L. The Complex Energy Landscape of the Protein IscU. *Biophys. J.* **2015**, *109*, 1019−1025.
(40) Shan, B.; McClendon, S.; Rospigliosi, C.; Eliezer, D.; Raleigh, D. P. The Cold Denatured State of the C-Terminal Domain of Protein L9 Is Compact and Contains Both Native and Non-Native Structure. *J. Am. Chem. Soc.* **2010**, *132*, 4669−4677.
(41) Luan, B.; Shan, B.; Baiz, C.; Tokmakoff, A.; Raleigh, D. P. Cooperative Cold Denaturation: The Case of the C-Terminal Domain of Ribosomal Protein L9. *Biochemistry* **2013**, *52*, 2402−2409.
(42) Stenzoski, N. E.; Luan, B.; Holehouse, A. S.; Raleigh, D. P. The Unfolded State of the C-Terminal Domain of L9 Expands at Low but Not at Elevated Temperatures. *Biophys. J.* **2018**, *115*, 655−663.
(43) Stenzoski, N. E.; Zou, J.; Piserchio, A.; Ghose, R.; Holehouse, A. S.; Raleigh, D. P. The Cold-Unfolded State Is Expanded but Contains Long-and Medium-Range Contacts and Is Poorly Described by Homopolymer Models. *Biochemistry* **2020**, *59*, 3290−3299.
(44) Adrover, M.; Esposito, V.; Martorell, G.; Pastore, A.; Temussi, P. A. Understanding Cold Denaturation: The Case Study of Yfh1. *J. Am. Chem. Soc.* **2010**, *132*, 16240−16246.
(45) Adrover, M.; Martorell, G.; Martin, S. R.; Urosev, D.; Konarev, P. V.; Svergun, D. I.; Daura, X.; Temussi, P.; Pastore, A. The Role of Hydration in Protein Stability: Comparison of the Cold and Heat Unfolded States of Yfh1. *J. Mol. Biol.* **2012**, *417*, 413−424.
(46) Sanfelice, D.; Puglisi, R.; Martin, S. R.; Di Bari, L.; Pastore, A.; Temussi, P. A. Yeast Frataxin Is Stabilized by Low Salt Concentrations: Cold Denaturation Disentangles Ionic Strength Effects from Specific Interactions. *PLoS One* **2014**, *9*, No. e95801.
(47) Rösner, H. I.; Caldarini, M.; Prestel, A.; Vanoni, M. A.; Broglia, R. A.; Aliverti, A.; Tiana, G.; Kragelund, B. B. Cold Denaturation of the HIV-1 Protease Monomer. *Biochemistry* **2017**, *56*, 1029−1032.
(48) Leman, J. K.; Weitzner, B. D.; Lewis, S. M.; Adolf-Bryfogle, J.; Alam, N.; Alford, R. F.; Aprahamian, M.; Baker, D.; Barlow, K. A.; Barth, P.; et al. Macromolecular Modeling and Design in Rosetta: Recent Methods and Frameworks. *Nat. Methods* **2020**, *17*, 665−680.
(49) Murphy, G. S.; Mills, J. L.; Miley, M. J.; Machius, M.; Szyperski, T.; Kuhlman, B. Increasing Sequence Diversity with Flexible Backbone Protein Design: The Complete Redesign of a Protein Hydrophobic Core. *Structure* **2012**, *20*, 1086−1096.
(50) Maguire, J. B.; Boyken, S. E.; Baker, D.; Kuhlman, B. Rapid Sampling of Hydrogen Bond Networks for Computational Protein Design. *J. Chem. Theory Comput.* **2018**, *14*, 2751−2760.
(51) Feller, G. Psychrophilic Enzymes: From Folding to Function and Biotechnology. *Scientifica* **2013**, *2013*, 1−28.
(52) Maguire, J. B.; Haddox, H. K.; Strickland, D.; Halabiya, S. F.; Coventry, B.; Griffin, J. R.; Pulavarti, S. V. S. R. K.; Cummins, M.; Thieker, D. F.; Klavins, E.; et al. Perturbing the Energy Landscape for Improved Packing during Computational Protein Design. *Proteins* **2021**, *89*, 436−449.
(53) Mangiagalli, M.; Brocca, S.; Orlando, M.; Lotti, M. The "Cold Revolution". Present and Future Applications of Cold-Active Enzymes and Ice-Binding Proteins. *New Bio Technol.* **2020**, *55*, 5−11.
(54) Kuhlman, B.; Baker, D. Native Protein Sequences Are Close to Optimal for Their Structures. *Proc. Natl. Acad. Sci. U.S.A.* **2000**, *97*, 10383−10388.
(55) Boyken, S. E.; Chen, Z.; Groves, B.; Langan, R. A.; Oberdorfer, G.; Ford, A.; Gilmore, J. M.; Xu, C.; Dimaio, F.; Pereira, J. H.; et al. De Novo Design of Protein Homo-oligomers with Modular Hydrogen-Bond Network-Mediated Specificity. *Science* **2016**, *352*, 680−687.
(56) O'Meara, M. J.; Leaver-Fay, A.; Tyka, M. D.; Stein, A.; Houlihan, K.; DiMaio, F.; Bradley, P.; Kortemme, T.; Baker, D.; Snoeyink, J.; Kuhlman, B. Combined Covalent-Electrostatic Model of Hydrogen Bonding Improves Structure Prediction with Rosetta. *J. Chem. Theory Comput.* **2015**, *11*, 609−622.
(57) Abraham, M. J.; Murtola, T.; Schulz, R.; Páll, S.; Smith, J. C.; Hess, B.; Lindahl, E. Gromacs: High Performance Molecular Simulations through Multi-Level Parallelism from Laptops to Supercomputers. *SoftwareX* **2015**, *1−2*, 19−25.
(58) Vega, C.; Abascal, J. L. F.; Nezbeda, I. Vapor-Liquid Equilibria from the Triple Point up to the Critical Point for the New Generation of TIP4P-like Models: TIP4P/Ew, TIP4P/2005, and TIP4P/Ice. *J. Chem. Phys.* **2006**, *125*, 034503.
(59) Kim, S. B.; Palmer, J. C.; Debenedetti, P. G. Computational Investigation of Cold Denaturation in the Trp-Cage Miniprotein. *Proc. Natl. Acad. Sci. U.S.A.* **2016**, *113*, 8991−8996.
(60) Bussi, G.; Donadio, D.; Parrinello, M. Canonical Sampling through Velocity Rescaling. *J. Chem. Phys.* **2007**, *126*, 014101.
(61) Parrinello, M.; Rahman, A. Polymorphic Transitions in Single Crystals: A New Molecular Dynamics Method. *J. Appl. Phys.* **1981**, *52*, 7182−7190.
(62) Humphrey, W.; Dalke, A.; Schulten, K. VMD: Visual Molecular Dynamics. *J. Mol. Graph.* **1996**, *14*, 33−38.
(63) Otwinowski, Z.; Minor, W. Processing of X-Ray Diffraction Data Collected in Oscillation Mode. *Methods Enzymol.* **1997**, *276*, 307−326.
(64) Findeisen, M.; Brand, T.; Berger, S. A 1H-NMR Thermometer Suitable for Cryoprobes. *Magn. Reson. Chem.* **2007**, *45*, 175−178.
(65) Smolsky, I. L.; Liu, P.; Niebuhr, M.; Ito, K.; Weiss, T. M.; Tsuruta, H. Biological Small-Angle X-Ray Scattering Facility at the Stanford Synchrotron Radiation Laboratory. *J. Appl. Crystallogr.* **2007**, *40*, s453−s458.
(66) Manalastas-Cantos, K.; Konarev, P. V.; Hajizadeh, N. R.; Kikhney, A. G.; Petoukhov, M. V.; Molodenskiy, D. S.; Panjkovich, A.; Mertens, H. D. T.; Gruzinov, A.; Borges, C.; et al. ATSAS 3.0: Expanded Functionality and New Tools for Small-Angle Scattering Data Analysis. *J. Appl. Crystallogr.* **2021**, *54*, 343−355.
(67) Lopez, M. M.; Makhatadze, G. I. Differential Scanning Calorimetry. *Methods Mol. Biol.* **2002**, *173*, 113−119.
(68) Kuhlman, B.; Raleigh, D. P. Global analysis of the thermal and chemical denaturation of the N-terminal domain of the ribosomal protein L9 in H2O and D2O. Determination of the thermodynamic parameters, ΔH°, ΔS°, and $\Delta C^\circ p$, and evaluation of solvent isotope effects. *Protein Sci.* **1998**, *7*, 2405−2412.
(69) Spolar, R. S.; Livingstone, J. R.; Record, M. T. Use of Liquid Hydrocarbon and Amide Transfer Data to Estimate Contributions to Thermodynamic Functions of Protein Folding from the Removal of Nonpolar and Polar Surface from Water. *Biochemistry* **1992**, *31*, 3947−3955.
(70) Fleming, P. J.; Fleming, K. G. HullRad: Fast Calculations of Folded and Disordered Protein and Nucleic Acid Hydrodynamic Properties. *Biophys. J.* **2018**, *114*, 856−869.
(71) Carugo, O. Statistical Survey of the Buried Waters in the Protein Data Bank. *Amino Acids* **2016**, *48*, 193−202.
(72) Carugo, O. Structure and Function of Water Molecules Buried in the Protein Core. *Curr. Protein Pept. Sci.* **2015**, *16*, 259−265.
(73) Klamt, A.; Nagarathinam, K.; Tanabe, M.; Kumar, A.; Balbach, J. Hyperbolic Pressure-Temperature Phase Diagram of the Zinc-Finger Protein ApoKti11 Detected by NMR Spectroscopy. *J. Phys. Chem. B* **2019**, *123*, 792−801.
(74) Cierpicki, T.; Otlewski, J. Amide Proton Temperature Coefficients as Hydrogen Bond Indicators in Proteins. *J. Biomol. NMR* **2001**, *21*, 249−261.
(75) Micsonai, A.; Wien, F.; Kernya, L.; Lee, Y. H.; Goto, Y.; Réfrégiers, M.; Kardos, J. Accurate Secondary Structure Prediction and Fold Recognition for Circular Dichroism Spectroscopy. *Proc. Natl. Acad. Sci. U.S.A.* **2015**, *112*, E3095−E3103.
(76) Micsonai, A.; Wien, F.; Bulyáki, É.; Kun, J.; Moussong, É.; Lee, Y.-H.; Goto, Y.; Réfrégiers, M.; Kardos, J. BeStSel: A Web Server for Accurate Protein Secondary Structure Prediction and Fold Recognition from the Circular Dichroism Spectra. *Nucleic Acids Res.* **2018**, *46*, W315−W322.

https://doi.org/10.1021/acs.jpcb.1c10750
J. Phys. Chem. B 2022, 126, 1212−1231

(77) Kuhlman, B.; Yang, H. Y.; Boice, J. A.; Fairman, R.; Raleigh, D. P. An Exceptionally Stable Helix from the Ribosomal Protein L9: Implications for Protein Folding and Stability. *J. Mol. Biol.* **1997**, *270*, 640−647.
(78) Richardson, J. M.; Makhatadze, G. I. Temperature Dependence of the Thermodynamics of Helix-Coil Transition. *J. Mol. Biol.* **2004**, *335*, 1029−1037.
(79) Kelly, S.; Price, N. The Use of Circular Dichroism in the Investigation of Protein Structure and Function. *Curr. Protein Pept. Sci.* **2000**, *1*, 349−384.
(80) Sreerama, N.; Manning, M. C.; Powers, M. E.; Zhang, J.-X.; Goldenberg, D. P.; Woody, R. W. Tyrosine, Phenylalanine, and Disulfide Contributions to the Circular Dichroism of Proteins: Circular Dichroism Spectra of Wild-Type and Mutant Bovine Pancreatic Trypsin Inhibitor. *Biochemistry* **1999**, *38*, 10814−10822.
(81) Woody, R. W. Circular dichroism. *Methods Enzymol.* **1995**, *246*, 34−71.
(82) Vivian, J. T.; Callis, P. R. Mechanisms of Tryptophan Fluorescence Shifts in Proteins. *Biophys. J.* **2001**, *80*, 2093−2109.
(83) Royer, A. Fluorescence Spectroscopy. *Methods Mol. Biol.* **1995**, *40*, 65−89.
(84) Callis, P. R. Simulating Electrostatic Effects on Electronic Transitions in Proteins. *Mol. Simul.* **2015**, *41*, 190−204.
(85) Sjöberg, B.; Pap, S.; Sjöberg, B.; Pap, S. The Temperature Properties of Human A2-Macroglobulin in the Range −15 to +37°C. An Investigation of Supercooled Solutions Using Small-Angle X-Ray Scattering and Dilatometry. *Int. J. Biol. Macromol.* **1985**, *7*, 219−222.
(86) Sun, T.; Lin, F.-H.; Campbell, R. L.; Allingham, J. S.; Davies, P. L.; Davies, P. L. An Antifreeze Protein Folds with an Interior Network of More than 400 Semi-Clathrate Waters. *Science* **2014**, *343*, 795−798.
(87) Rambo, R. P.; Tainer, J. A. Accurate Assessment of Mass, Models and Resolution by Small-Angle Scattering. *Nature* **2013**, *496*, 477−481.
(88) Johnson, C. S. Diffusion Ordered Nuclear Magnetic Resonance Spectroscopy: Principles and Applications. *Prog. Nucl. Magn. Reson. Spectrosc.* **1999**, *34*, 203−256.
(89) De La Torre, J. G.; Huertas, M. L.; Carrasco, B. HYDRONMR: Prediction of NMR Relaxation of Globular Proteins from Atomic-Level Structures and Hydrodynamic Calculations. *J. Magn. Reson.* **2000**, *147*, 138−146.
(90) Wilkins, D. K.; Grimshaw, S. B.; Receveur, V.; Dobson, C. M.; Jones, J. A.; Smith, L. J. Hydrodynamic Radii of Native and Denatured Proteins Measured by Pulse Field Gradient NMR Techniques. *Biochemistry* **1999**, *38*, 16424−16431.
(91) Makhatadze, G. I.; Privalov, P. L. Heat Capacity of Proteins I. Partial Molar Heat Capacity of Individual Amino Acid Residues in Aqueous Solution: Hydration Effect. *J. Mol. Biol.* **1990**, *213*, 375−384.
(92) Seelig, J. Cooperative Protein Unfolding. A Statistical-Mechanical Model for the Action of Denaturants. *Biophys. Chem.* **2018**, *233*, 19−25.
(93) Serrano, L.; Sancho, J.; Hirshberg, M.; Fersht, A. R. α-Helix Stability in Proteins. I. Empirical Correlations Concerning Substitution of Side-Chains at the N and C-Caps and the Replacement of Alanine by Glycine or Serine at Solvent-Exposed Surfaces. *J. Mol. Biol.* **1992**, *227*, 544−559.
(94) López-Llano, J.; Campos, L. A.; Sancho, J.; Sancho, J. α-Helix Stabilization by Alanine Relative to Glycine: Roles of Polar and Apolar Solvent Exposures and of Backbone Entropy. *Proteins Struct. Funct. Genet.* **2006**, *64*, 769−778.
(95) Pace, C. N.; Scholtz, J. M. A Helix Propensity Scale Based on Experimental Studies of Peptides and Proteins. *Biophys. J.* **1998**, *75*, 422−427.
(96) Makhatadze, G. I. Thermodynamics Of α-Helix Formation. *Adv. Protein Chem.* **2005**, *72*, 199−226.
(97) Alfano, C.; Sanfelice, D.; Martin, S. R.; Pastore, A.; Temussi, P. A. An Optimized Strategy to Measure Protein Stability Highlights Differences between Cold and Hot Unfolded States. *Nat. Commun.* **2017**, *8*, 15428.
(98) Rose, G. D. Protein Folding - Seeing Is Deceiving. *Protein Sci.* **2021**, *30*, 1606−1616.
(99) Angell, C. A. Supercooled Water. *Annu. Rev. Phys. Chem.* **1983**, *34*, 593−630.
(100) Sanfelice, D.; Morandi, E.; Pastore, A.; Niccolai, N.; Temussi, P. A. Cold Denaturation Unveiled: Molecular Mechanism of the Asymmetric Unfolding of Yeast Frataxin. *ChemPhysChem* **2015**, *16*, 3599−3602.
(101) Sánchez, I. E.; Kiefhaber, T. Non-Linear Rate-Equilibrium Free Energy Relationships and Hammond Behavior in Protein Folding. *Biophys. Chem.* **2003**, *100*, 397−407.
(102) Plaxco, K. W.; Simons, K. T.; Baker, D. Contact Order, Transition State Placement and the Refolding Rates of Single Domain Proteins. *J. Mol. Biol.* **1998**, *277*, 985−994.
(103) Szyperski, T. Room Temperature X-Ray Crystallography Reveals Conformational Heterogeneity of Engineered Proteins. *Structure* **2017**, *25*, 691−692.
(104) Sathyamoorthy, B.; Singarapu, K. K.; Garcia, A. E.; Szyperski, T. Protein Conformational Space Populated in Solution Probed with Aromatic Residual Dipolar (13) C-(1) H Couplings. *Chembiochem* **2013**, *14*, 684−688.
(105) Matysiak, S.; Debenedetti, P. G.; Rossky, P. J. Role of Hydrophobic Hydration in Protein Stability: A 3D Water-Explicit Protein Model Exhibiting Cold and Heat Denaturation. *J. Phys. Chem. B* **2012**, *116*, 8095−8104.
(106) Arsiccio, A.; Shea, J.-E. Protein Cold Denaturation in Implicit Solvent Simulations: A Transfer Free Energy Approach. *J. Phys. Chem. B* **2021**, *125*, 5222−5232.
(107) Ikenoue, T.; Lee, Y.-H.; Kardos, J.; Saiki, M.; Yagi, H.; Kawata, Y.; Goto, Y. Cold Denaturation of α-Synuclein Amyloid Fibrils. *Angew. Chem., Int. Ed.* **2014**, *53*, 7799−7804.
(108) Edwards, R. J.; Mansouri, K.; Stalls, V.; Manne, K.; Watts, B.; Parks, R.; Janowska, K.; Gobeil, S. M. C.; Kopp, M.; Li, D.; et al. Cold Sensitivity of the SARS-CoV-2 Spike Ectodomain. *Nat. Struct. Mol. Biol.* **2021**, *28*, 128−131.
(109) Yang, T.-J.; Yu, P.-Y.; Chang, Y.-C.; Hsu, S.-T. D. D614G Mutation in the SARS-CoV-2 Spike Protein Enhances Viral Fitness by Desensitizing It to Temperature-Dependent Denaturation. *J. Biol. Chem.* **2021**, *297*, 101238.
(110) Tendulkar, S.; Hattiholi, A.; Chavadar, M.; Dodamani, S. Psychrophiles: A Journey of Hope. *J. Biosci.* **2021**, *46*, 64.

https://doi.org/10.1021/acs.jpcb.1c10750
J. Phys. Chem. B 2022, 126, 1212−1231